Czech Technical University in Prague
Faculty of Nuclear Sciences and Physical Engineering

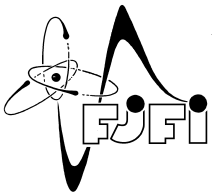

Development of an algorithm for linear particle track reconstruction in SuperNEMO detector

Vývoj algoritmu pro rekonstrukci lineárních drah částic v SuperNEMO detektoru

Bachelor's Degree Project

Author: **Tomáš Křižák**

Supervisor: **Mgr. Miroslav Macko, Ph.D.**

Academic year: 2022/2023

Katedra: matematiky Akademický rok: 2022/2023

ZADÁNÍ BAKALÁŘSKÉ PRÁCE

Student:	Tomáš Křižák
Studijní program:	Aplikace přírodních věd
Studijní obor:	Matematické inženýrství
Studijní zaměření:	Matematické modelování
Název práce (česky):	Vývoj algoritmu pro rekonstrukci lineárních drah částic v SuperNEMO detektoru
Název práce (anglicky):	Development of an algorithm for linear particle track reconstruction in SuperNEMO detector

Pokyny pro vypracování:

1) Seznamte se s projektem SuperNEMO, s jeho designem, jeho fyzikálními cíli a jeho významem v rámci neutrinové fyziky [1].
2) Naučte se zpracovávat data ze SuperNEMO detektoru. Osvojte si principy analýzy dat zejména z dráhového detektoru.
3) Seznamte se s již řešenými problémy hledání fitů pomocí Legendreovy transformace [2, 3].
4) Napište jednoduchý skript schopný rekonstrukce rovných drah z dat ze SuperNEMO detektoru (detektor bez magnetického pole).
5) Napište software schopný vizualizovat třírozměrný zjednodušený model SuperNEMO detektoru, který umožní prohlížet data událost za událostí.
6) Dokažte funkčnost vašeho fitovacího algoritmu na uměle vygenerovaných dokonalých datech (bez nepřesností). Následně aplikujte skript na reálná data ze SuperNEMO detektoru.
7) Prezentujte dosažené výsledky v rámci mezinárodní kolaborace SuperNEMO.

Doporučená literatura:

1) R. Arnold, et al., Probing new physics models of neutrinoless double beta decay with SuperNEMO. Eur. Phys. J. C 70, 2010, 927–943.

2) T. Alexopoulos, et al., Track reconstruction through the application of the Legendre Transform on ellipses. arXiv:1605.04738v1, 2016.

3) T. Alexopoulos, et al., Identification of circles from datapoints using the Legendre transform. Nuclear Instruments and Methods in Physics Research Section A: Accelerators, Spectrometers, Detectors and Associated Equipment 745, 2014, 16-23.

Jméno a pracoviště vedoucího bakalářské práce:

Mgr. Miroslav Macko, Ph.D.
ÚTEF ČVUT v Praze, Husova 240/5, 110 00 Praha 1

Jméno a pracoviště konzultanta:

Datum zadání bakalářské práce: 31.10.2022

Datum odevzdání bakalářské práce: 2.8.2023

Doba platnosti zadání je dva roky od data zadání.

V Praze dne 31.10.2022

.....
garant oboru

.....
vedoucí katedry

.....
děkan

Acknowledgment:
I would like to thank my family and my girlfriend, who have always been a great support, not only during the writing of this work, but also during my whole studies. I am very grateful to my colleagues at IEAP CTU in Prague and the entire SuperNEMO Collaboration for welcoming me and allowing me to be a part of such an amazing project as SuperNEMO. However, my greatest thanks go to my friend and supervisor, Miroslav Macko, to whom I owe many of the skills I have learnt as he patiently guided me over the past three years.

Author's declaration:
I declare that this Bachelor's Degree Project is entirely my own work and I have listed all the used sources in the bibliography.

Prague, August 2, 2023 Tomáš Křižák

Název práce:

Vývoj algoritmu pro rekonstrukci lineárních drah částic v SuperNEMO detektoru

Autor: Tomáš Křižák

Obor: Matematické inženýrství

Zaměření: Matematické modelování

Druh práce: Bakalářská práce

Vedoucí práce: Mgr. Miroslav Macko, Ph.D. , Ústav technické a experimentální fyziky

Abstrakt: Hmotnost neutrina je jednou z největších otevřených otázek moderní částicové fyziky. Aby bylo možné změřit jeho hmotnost, spoléhá mnoho experimentů na měření poločasu takzvaného bezneutrinového dvojného beta rozpadu ($0\nu\beta\beta$). Experiment SuperNEMO vyniká v oblasti $0\nu\beta\beta$ díky svému jedinečnému tracko-calo designu, který slibuje nesrovnatelné možnosti redukce pozadí oproti jiným přístupům. K dosažení jeho plného potenciálu je však zapotřebí výkonného algoritmu pro rekonstrukci drah částic, který umožní hledaný rozpad detekovat.

V rámci předložené práce jsme vyvinuli první verzi softwaru pro rekonstrukci drah založeného na aplikaci Legendrovy transformace. V této práci demonstrujeme jeho sílu a možnosti vylepšení.

Klíčová slova: bezneutrinový dvojný beta rozpad, Legendreova transformace, neutrinová fyzika, SuperNEMO, rekonstrukce drah

Title:

Development of an algorithm for linear particle track reconstruction in SuperNEMO detector

Author: Tomáš Křižák

Abstract: The mass of the neutrino is one of the biggest open questions in modern particle physics. In order to measure its mass, many experiments rely on measuring the half-life of a predicted decay called neutrinoless double beta decay ($0\nu\beta\beta$). The SuperNEMO experiment stands out in the field of $0\nu\beta\beta$ thanks to its unique tracko-calo design, which promises background rejection capabilities unmatched by other approaches. However, to reach its full potential, a powerful reconstruction algorithm is needed in order to detect the elusive decay.

Withing the presented work, we have developed the first version of the reconstruction software based on the application of the Legendre transform. In the thesis we demonstrate its power and the opportunities for improvement.

Key words: Legendre transform, neutrinoless double beta decay, neutrino physics, SuperNEMO, track reconstruction

Contents

List of Figures

Introduction

About fifty years ago, the most detailed and successful model of atomic world to date has been introduced to the world, the Standard Model (SM). It describes our world as an interplay of 17 elementary particles and it has withstood many challenges over the years. For decades, it has successfully described known particles, but also predicted new particles that were later confirmed experimentally. However, we know that SM is simply not enough to describe the physics in its entirety. For example, it cannot describe and explain gravity, the observed expansion of the universe, or baryon asymmetry. To progress further in our understanding we must search beyond the scope of the SM.

One of the most promising candidates to make step beyond the SM is the neutrino. Neutrinos are elementary particles that come in three flavours: electron neutrino, muon neutrino and tau neutrino. In 2015, the Nobel Prize in Physics was awarded for the experimental discovery of neutrino oscillation, which describes how neutrinos can change their flavour. This discovery implies that neutrinos have mass, contrary to the SM. However, a question arises as to what the masses of the three possible neutrino mass states are.

In 1935, Maria Goeppert-Mayer proposed the existence of a decay called double beta decay. Double beta decay is an extremely rare process, in which two neutrons turn into protons, emitting two electrons and two antineutrinos. This process has been experimentally proven to exist among several isotopes. However, assuming that the neutrino is its own antiparticle (so-called Majorana particle), another version of this decay could exist, neutrinoless double beta decay ($0\nu\beta\beta$), where no antineutrinos are emitted. In this mode of double beta decay, the half-life of the process depends on the so-called effective neutrino mass. This means that $0\nu\beta\beta$ could help to finally measure the masses of the neutrinos.

In general, the detection of $0\nu\beta\beta$ is pursued by two separate families of experiments based on the design of the detectors. The first group are experiments where the detector itself behaves as a potential source of $0\nu\beta\beta$, for example the GERDA, MAJORANA or EXO experiments. The second group are experiments where the source isotope is separated from the detection part of the detector. This design was utilized by NEMO-3 experiment and now by its successor, SuperNEMO.

In the centre of SuperNEMO, a thin foil made of a total of 6.11 kg of enriched ^{82}Se acts as the source of $0\nu\beta\beta$. The source foil is surrounded by a tracking detector, a part of the detector that makes the design of SuperNEMO unique. Its purpose is to track passing particles and reconstruct their trajectories. Electrons emitted from source foil, as well as other unwanted particles are in the end absorbed by calorimeter, a part of the detector, which goal is to accurately measure the particles energy. With combined information from tracker and calorimeter about geometry and energy of each event we are able to distinguish $0\nu\beta\beta$ from other types of events.

The tracker is an airtight chamber filled with helium and small amount of ethanol and argon. Inside this chamber is a grid of 2034 tracker cells in Geiger mode. Each one consists of an

anode wire under high voltage in the middle, field shaping wires on the sides of the cell and two cathode caps on the top and bottom of the cell. When a charged particle passes through a given tracker cell it ionises the gas inside, creating an avalanche of particles that influences the voltage of the anode wire and cathodes providing us information about the distance of the passing particle to the anode wire as well as distance to the cathodes. With data from several tracker cells triggered by the same particle we should be able to reconstruct the entire trajectory of this particle. However, a successful assembly of all the information into the correct trajectory requires a development of a powerful reconstruction algorithm.

This thesis aims to investigate the challenges involved in this problem, explore the potential of using Legendre transformation in trajectory reconstruction, and ultimately develop a functional algorithm capable of reconstructing linear particle trajectories from real data obtained from the SuperNEMO experiment.

Chapter 1 summarizes history of neutrino physics and neutrinoless double beta decay and different experiment designs used in the search of this decay.

Chapter 2 focuses on a more detailed description of the design of SuperNEMO demonstrator and its individual components.

Chapter 3 explains the convenience of Legendre transform for reconstruction of linear paths from data obtained by SuperNEMO and demonstrates effectiveness of this approach on simulated data without measurement errors.

Chapter 4 describes the difficulties of raw SuperNEMO data and our dedicated C++ library to work with them. Finally, it demonstrates usage of Legendre transform in reconstruction of the real data taken by the SuperNEMO demonstrator.

Chapter 1

Basics of neutrino physics

1.1 The Standard Model and beyond

In the 5^{th} century BCE, Democritus, an ancient Greek philosopher, first used the word "atomos", which means "indivisible". He suggested that the world around us is made of tiny indivisible particles, basic building blocks of everything, but it took more than two millennia to prove him right. With the discovery of atoms, we understood that our world is really made of tiny building blocks. However, we did not yet understand much about them. In 1897, while studying cathode rays, Joseph J. Thomson became the first person to discover the electron [1]. The electron is one of the fundamental particles of our universe, and today it is still considered indivisible. He proved that atoms are not indivisible as previously thought. Throughout the 20^{th} century, physicist discovered more of these basic building blocks. It took about half of a century until they were able to successfully describe these fundamental particles in a complex theoretical model that could predict how they behave, what are their properties and how they interact. We call this theory the Standard Model (the SM).

Not only could the SM describe what was already known but it also predicted the existence of new particles, such as the top quark [2], the tau neutrino [3] and, finally the Higgs boson [4]. The SM describes our world as an interplay of 12 different fundamental particles (6 quarks, 6 leptons), 4 force carrying bosons and the Higgs boson (Figure 1.1).

Even though, the SM is the most precise and complex description of the universe at the moment, it is obvious that the theory needs extensions. First of all, the SM does not include gravity at all. Einstein's theory of general relativity describes gravity very successfully but these two separate models are way too different to be put together into one "theory of everything". In 1933, astronomer Fritz Zwicky was observing Coma cluster of galaxies. He calculated that the total mass of the stars inside the cluster is not sufficient to generate gravitational field large enough to keep the cluster together. He suggested a presence of unknown matter that interacts via gravity as normal matter. He named it "the Dark Matter" [6]. The Dark Matter is another mystery left unexplained by the SM.

The SM is incredibly successful, however, it does not provide answers to all opened questions of particle physics. We know that there exists unknown physics beyond the SM. One possible bridge towards this new understanding might lead through the study of neutrino.

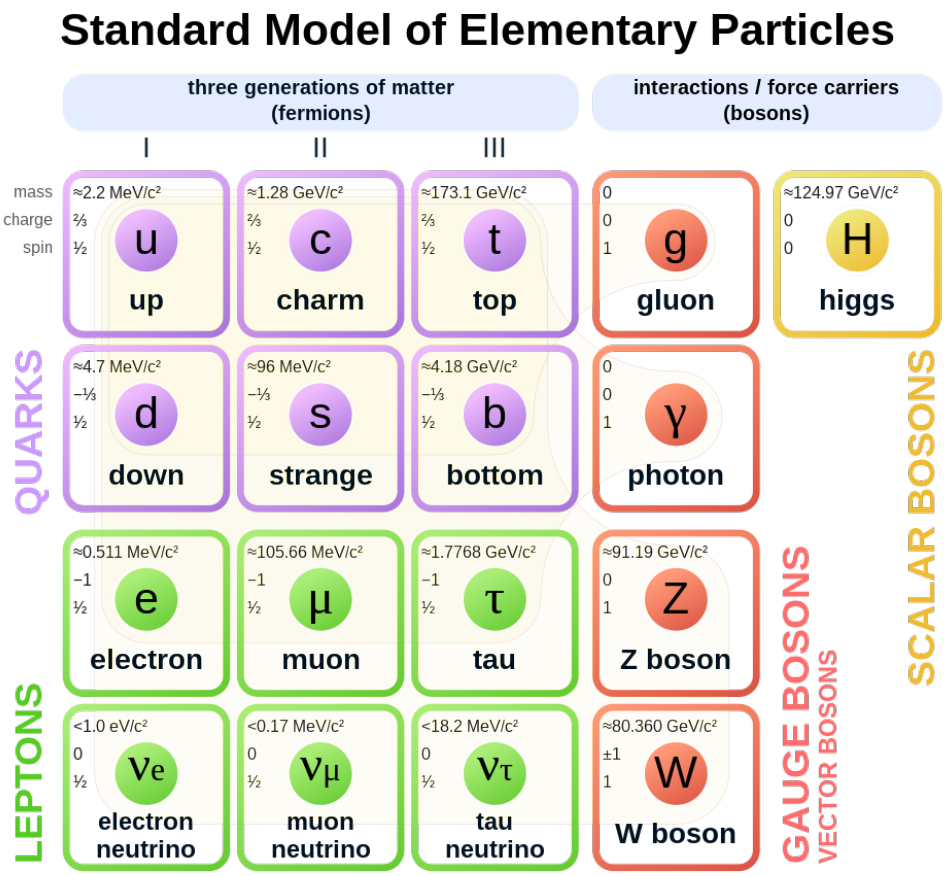

Figure 1.1: Particles of the Standard Model [5]

1.2 Neutrino and its history

In 1899, Ernest Rutherford discovered two types of radioactivity, one composed of less penetrating particles, which he called the alpha decay, and another composed of more penetrating particles that he named the beta decay. These two, together with gamma radiation, are the most common radioactive processes. When physicists were studying beta decay they stumbled into a problem. It seemed to break the law of energy conservation.

Each spontaneous decay should release exactly the same amount of energy equal to the difference between binding energy of initial and final nuclei (so called Q-value). This was experimentally observed for alpha and gamma decay but beta decay seemed to act differently. The spectrum of kinetic energy of the electron did not have a form of a sharp delta peak but rather a form of continuous distribution of various energies. To explain this, Wolfgang Pauli suggested an existence of a neutral light particle. In his famous letter to conference participants in Tübingen, he explained his idea [7]. The particle carries the rest of the decay energy but rarely interacts with regular matter, therefore, is very difficult to measure. That would explain the presence of continuous spectrum but it would be hard to prove experimentally. Pauli originally named the particle "neutron" but this name was given to the neutral nucleon discovered in 1932. Finally, the name neutrino, as an Italian diminutive of the word neutron, was later accepted. Pauli expected that the neutrino would never be detected.

After another 26 years, in 1956, Clyde Cowan and Frederick Reines proved the existence of neutrino [8] by searching for a theoretically predicted process called inverse beta decay:

$$\bar{\nu}_e + p^+ \rightarrow n^0 + e^+. \tag{1.1}$$

In this process, an electron antineutrino is captured by a proton in the nucleus and emits a neutron and a positron. The positron annihilates and creates a gamma pair with a signature energy of 511 keV each. After a short time, the neutron is captured in ^{108}Cd (see the description of the setup below) and the nucleus deexcites by emission of one or multiple gammas. The emitted gammas can be detected.

In their setup, two tanks with a total volume of 200 l were utilized as a target for the electron antineutrinos. They added 40 kg of cadmium chloride to capture the emitted neutrons. To detect the emitted gammas, they used tanks of liquid scintillator around the water tanks. They built the detector conveniently near a nuclear reactor. That allowed them to compare the measured neutrino fluxes with the reactor turned on and off. They managed to measure an increase of number of emitted particles, proving the existence of neutrinos.

Neutrinos have zero electromagnetic charge, therefore, they are invisible to our detection systems. Nevertheless, they can be detected indirectly. The neutrinos are always appearing in the weak processes along with one of the charged leptons - electron, muon or tau. The detection of these three leptons is, therefore, crucial when we are trying to reconstruct the presence of neutrino. Due to this fact, we recognize three so-called flavours of neutrinos. Electron neutrino always appears with electrons in the process. In 1962, new type of neutrino was discovered [9], muon neutrino, which was already predicted in 1940. Last known flavour is tau neutrino [3]. Similarly to the other fermions, the neutrinos also have their own antiparticle variant called antineutrinos.

After their experimental confirmation, neutrinos turned out to be even more puzzling than previously thought. Raymond Davis, Jr. and John Bahcall wanted to measure flux of neutrinos coming from the Sun, which should contain uniquely the electron neutrinos as they originate in the beta decay. Based on their calculations, they anticipated to observe 9.3 ± 1.3 SNU[1] but measured only 2.56 ± 0.32 SNU [10]. This issue went down in history as the Solar Neutrino Problem and turned out to play a major role on the way to understand neutrinos.

Today we know that the neutrinos exist in a form of a mixture of all its flavours. First similar ideas were proposed already in 1958 by Bruno Pontecorvo [11]. The key idea was that the composition of this mixture can change as the neutrinos fly through space. If the neutrino contains more of the electron flavour in its composition, it is more likely to interact with electrons and so on. What was created purely as an electron neutrino in the Sun, could change its flavour as it travels towards the Earth and could potentially interact with particles other than electrons. Such effect could explain the observed lack of measured solar neutrinos.

Existence of this process would have non-trivial implications. The SM assumes neutrinos to be massless as it is good enough approximation for high energy experiments. However, for neutrino oscillations to be possible, the different flavours of neutrinos need to have different masses. This means that the existence of neutrino oscillations would prove that neutrinos have mass.

Similar to the flavour states, we recognize three neutrino mass states. In general, a neutrino mass state does not correspond to a neutrino flavour state. The relation between flavour states

[1] 1 SNU (solar neutrino unit) is equal to 10^{36} neutrino captures per second

$|\nu_e\rangle, |\nu_\mu\rangle, |\nu_\tau\rangle$ and mass states $|\nu_1\rangle, |\nu_2\rangle, |\nu_3\rangle$ is described by so-called PMNS matrix (Pontecorvo – Maki – Nakagawa – Sakata matrix):

$$|\nu_\alpha\rangle = \sum_i U_{\alpha i}|\nu_i\rangle. \tag{1.2}$$

To understand why does the existence of oscillations require non-zero mass differences between different mass states, we can look at a simplified case of oscillations between only two neutrino states. In this simplified case the PMNS matrix can be parametrised by a single parameter θ, so-called mixing angle:

$$\begin{pmatrix}|\nu_\alpha\rangle\\|\nu_\beta\rangle\end{pmatrix} = \begin{pmatrix}\cos\theta & \sin\theta\\ -\sin\theta & \cos\theta\end{pmatrix}\begin{pmatrix}|\nu_1\rangle\\|\nu_2\rangle\end{pmatrix} \tag{1.3}$$

The probability of oscillation of ultrarelativistic neutrino between two states $|\nu_\alpha\rangle$ and $|\nu_\beta\rangle$ can be calculated by following formula [12]:

$$P(\nu_\alpha \to \nu_\beta) = \sin^2(2\theta)\sin^2\left(\frac{\Delta m^2_{ij} L}{4E}\right), \tag{1.4}$$

where L is the traveled distance, E is energy of this neutrino and Δm^2_{ij} is a difference of squared masses of the two mass states.

In order to test this theory, a new generation of neutrino detectors had to be built. This is because all the previous experiments only detected electron neutrinos. Experiment Super-Kamiokande was the first experiment to collect evidence of neutrino oscillation while observing atmospheric muon neutrinos changing into tau neutrinos [13]. In 1999, Sudbury Neutrino Observatory was able to compare numbers of neutrinos of all flavours with only electron neutrinos emitted from decay of ^{8}B in the Sun. With their combined results, they successfully confirmed the existence of neutrino oscillations.

Experimental confirmation that neutrino oscillation has a non-zero probability together with Equation 1.4 has two major implications. First, it is obvious that the mixing angle has to be non-zero. For the 3-state case it means that the PMNS matrix is not an identity matrix, and therefore, the neutrinos are mixing. Second, the mass difference has to be non-zero as well, which proves that at least two of the three neutrinos mass states have non-zero mass. The Nobel Prize in physics in 2015 was awarded to Takaaki Kajita and Arthur B. McDonald for this discovery.

1.3 Neutrinoless double beta decay

In 1935, Maria Goeppert-Mayer proposed the existence of a decay called double beta decay (DBD) [14]. The general term DBD includes several different modes but the most commonly discussed is its double electron emission ($2\nu\beta\beta$). $2\nu\beta\beta$ is a process in which two neutrons bound in a nucleus with even number of nucleons turn into two protons via emission of two electrons and two electron antineutrinos:

$$(A, Z) \to (A, Z+2) + 2e^- + 2\bar{\nu}_e \tag{1.5}$$

Maria Goeppert-Mayer also calculated the first theoretical estimates on frequency of this decay. In 1950, Mark Inghram and John Reynolds managed to indirectly confirm existence of

DBD of ^{130}Te with a radiochemical approach [15]. However, these radiochemical and geochemical methods were not reliable. The first direct observation of DBD was performed by a group led by Michael Moe in 1987 [16]. They measured this process in ^{82}Se and since then it has been successfully measured in several other isotopes.

If a nucleus can undergo two consecutive beta decays, it can also undergo DBD. However, DBD is quite rare compared to the ordinary beta decay, making it practically impossible to measure in most cases. Nonetheless, there are certain special instances where DBD can occur, but two consecutive beta decays are suppressed due to conservation of energy or unfavourable spin change.

When a nucleus undergoes a beta decay, its atomic weight A remains the same, but its atomic number Z changes. In other words, the number of nucleons (neutrons plus protons) stays constant, but the number of protons changes. In particle physics, we refer to nuclei with the same atomic weight as "isobars". These isobars have different binding energies and beta decay is only possible when the original nucleus has a higher binding energy than the resulting nucleus.

Binding energy of a nucleus can be understood as a quadratic function with respect to atomic weight. It contains an additional term that depends on the pairing of the spins of the nucleons. The nuclei prefer to have the protons and neutrons paired. There are three different possibilities of this pairing.

1. When both the number of neutrons (N) and protons (Z) are even (A is even), the binding energy is increased by a constant factor $\delta(N, Z)$.

2. When either N or Z are odd (A is odd), the additional term is zero.

3. When both N and Z are odd (A is even), the binding energy is decreased by a constant factor $\delta(N, Z)$.

In the case where a nucleus is from category 2 and undergoes beta decay it remains in category 2, and therefore the additional term stays the same. This means that all binding energies of these isobars lie on a single parabola – see Figure 1.2a. On the other hand, when a nucleus is from category 1 and undergoes beta decay, it becomes category 3, and vice versa. This leads to a difference in the additional pairing term and so the isobars with A even alter between two different parabolas – see figure 1.2b. Nuclei with even Z lie on the lower parabola, while the ones with odd Z on the upper parabola.

At points close to the minima of the parabolas, a nucleus with even atomic number can have lower energy then next nucleus in the beta decay chain. As a result, it cannot undergo this decay, and the only possible decay becomes DBD (Figure 1.2b). For this reason these special isotopes are ideal to be used in DBD experiments.

Shortly after $2\nu\beta\beta$ was proposed, Ettore Majorana suggested a new type of particles that would be their own antiparticles, now called "Majorana particles". In 1939, Wendell H. Furry showed that if neutrinos were Majorana particles, then another type of double beta decay would be possible, so-called neutrinoless double beta decay ($0\nu\beta\beta$) [18]. In this version, the two electron antineutrinos produced during $2\nu\beta\beta$ would not be created and only the two electrons would be emitted.

The process has not been observed yet. Nevertheless, the existence of such process would have important implications. Firstly, it would prove that neutrinos are really Majorana particles.

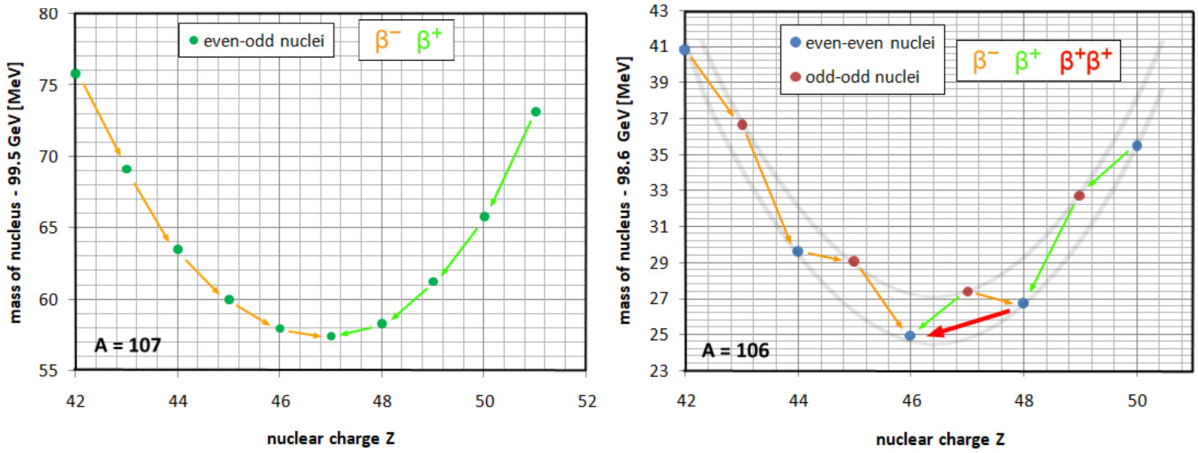

(a) Isobars of atomic mass 107

(b) Isobars of atomic mass 106

Figure 1.2: Plots showing binding energies of isobars of atomic mass 106 and 107. Green (β^+) and yellow (β^-) arrows represent possible beta decays into lower energy states. In plot (b) a nucleus with $Z = 48$ cannot undergo beta decay because the energy level of the nucleus with $Z = 47$ is higher. Red arrow between nuclei $Z = 48$ and $Z = 46$ represents double beta decay which is energetically possible. Graph taken from [17].

Today it remains the only possible way to prove their Majorana nature. Secondly, $0\nu\beta\beta$ causes lepton number violation. Lepton number is a quantum number describing whether a particle is a lepton (with lepton number 1), an antilepton (with lepton number -1) or whether is it not lepton (with lepton number 0). In all the processes we have observed so far, we observed a conservation of this quantum number. This means that whenever a lepton is created in some process, an antilepton must be created with it. In $0\nu\beta\beta$, two electrons are produced without antineutrinos so $0\nu\beta\beta$ can be understood as creation of matter without antimatter.

Finally, if $0\nu\beta\beta$ exists, its half-life can be used to determine neutrino masses. The half-life of $0\nu\beta\beta$ is directly related to the so-called effective neutrino mass:

$$\frac{1}{T^{0\nu}_{1/2}} \sim |m_{\beta\beta}|^2 G^{0\nu}(Q,Z)|M^{0\nu}|^2, \quad m_{\beta\beta} = \sum_{i=1}^{3} m_i U_{ei}^2 \tag{1.6}$$

where Q stands for the Q-value of $2\nu\beta\beta$, $G^{2\nu}(Q,Z)$ is kinematical phase space factor, $M^{0\nu}$ is a nuclear matrix element and effective neutrino mass $m_{\beta\beta}$ is given by a linear combination of neutrino masses.

1.4 Neutrinoless double beta decay experiments

Over the last few decades, many different detectors have been designed and constructed to measure the half-lives of $2\nu\beta\beta$ and $0\nu\beta\beta$. The value of half-life to which a given detector is sensitive can be calculated using the following formula [19]

$$T^{0\nu}_{1/2} \geq \alpha \left(\frac{a\epsilon}{W}\right) \sqrt{\frac{Mt}{b\delta E}}, \tag{1.7}$$

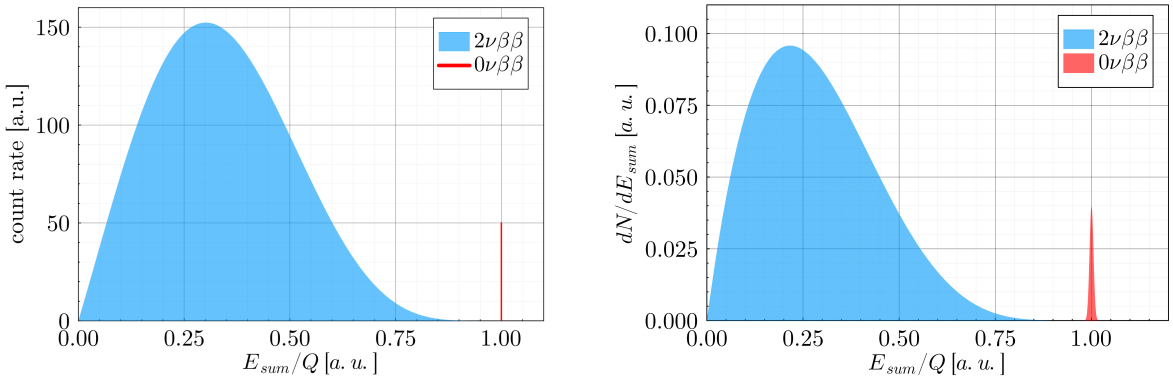

(a) Theoretical precise spectra

(b) Theoretical spectra with measurement errors

Figure 1.3: Approximation of a theoretical spectra of $2\nu\beta\beta$ and $0\nu\beta\beta$. X axis represents summed energy of emitted electrons relative to Q-value, Y axis in both plots represents relative probability. Plot (a) shows predicted spectra and plot (b) shows the spectra as viewed by a detector measuring with errors. Courtesy of Maroš Petro.

where $\alpha = 7.3 \times 10^{25}$ years, a is abundance of the DBD isotope in the observed sample, ϵ is the detection efficiency of the detector, M is the source mass in kg, t is the experimental running time in years, δE is the energy ROI (region of interest) of the $0\nu\beta\beta$ in keV and is proportional to the energy resolution of the detector and b is the rate of background counts in $\text{keV}^{-1}\text{kg}^{-1}\text{year}^{-1}$. These paramaters are crucial for a detector aiming to detect $0\nu\beta\beta$.

The $0\nu\beta\beta$ experiments are detecting the electrons emitted in the decay. The $0\nu\beta\beta$ candidate nuclei decay also via $2\nu\beta\beta$. In case of $2\nu\beta\beta$, the antineutrinos exit the detector without interaction, therefore the detector sees only two electrons from $2\nu\beta\beta$. The identification of the two electrons alone is not sufficient to distinguish between $2\nu\beta\beta$ and $0\nu\beta\beta$. Regardless of the process ($2\nu\beta\beta$ or $0\nu\beta\beta$) the structure of the nucleus before and after the decay is the same. Therefore, in the both processes, the same amount of energy (Q-value) is always released. During $2\nu\beta\beta$ a part of this energy is carried away by neutrinos which are not detected by the detector. The sum of the kinetic energies of the two electrons represents a remaining part of the decay energy. Therefore, it is following a continuous spectrum. In contrast, during $0\nu\beta\beta$ the entire Q-value transforms into the kinetic energy of two emitted electrons. This gives us a possibility to distinguish between $2\nu\beta\beta$ and $0\nu\beta\beta$ (Figure 1.3). For experiments which search for $0\nu\beta\beta$, energy resolution becomes very important in order to distinguish $0\nu\beta\beta$ from $2\nu\beta\beta$.

There are two main categories of $0\nu\beta\beta$ experiments based on their design. The first one is the detectors where the source isotope is the detector at the same time. These are called homogeneous detectors. The second category is detectors where source and detector systems are separated, so-called heterogeneous detectors.

1.4.1 Germanium experiments

First type of homogeneous detectors are semiconductor diode detectors. They aim to detect $0\nu\beta\beta$ of ^{76}Ge using Germanium semiconductors. When a particle interacts with the Germanium semiconductors, it produces charge carriers which are detected and turned into a voltage signal proportional to the deposited energy. These detectors have high detection efficiency and great resolution when using a cooling system. These detectors include experiments such as

Heidelberg-Moscow [20], MAJORANA [21] or GERDA (Germanium Detection Array) [22]. Another promising detector, LEGEND-1000 [23], with 1000kg of ^{76}Ge is currently under construction.

1.4.2 Bolometer experiments

Another type of homogeneous detectors are bolometer detectors. Bolometer detectors exploit change of heat capacity of a material at temperatures near absolute zero. When a particle is traveling through the detector volume, it deposits some amount of its energy. This energy heats the material of the detector and, thanks to the low heat capacity, even a very small amount of energy can affect the temperature. This temperature difference can be then measured using sensitive semiconductor thermistors. The difficulty of these experiments lies in the necessity of cooling down the source volume to under 10 mK. This type includes experiments like CUPID [24], CUORE [25] and LUCIFER [26] which aim to study $0\nu\beta\beta$ of ^{100}Mo, ^{130}Te and ^{82}Se respectively.

1.4.3 TPC and liquid scintillator experiments

In the category of homogeneous detectors we also identify projection chambers and liquid scintillator detectors. Time projection chambers use a sensitive volume of gas or liquid and a grid of anode wires. These anode wires create electric field thanks to which it is possible to reconstruct three-dimensional information about the trajectory of a particle moving through the sensitive volume. These detectors have better background rejection capabilities due to the ability to reconstruct the trajectories but worse energy resolution. One example of this type is EXO-200 [27] which focuses on $0\nu\beta\beta$ of ^{136}Xe using 200kg of Xenon. An important example of liquid scintillator experiments is KamLAND-Zen [28], originally a neutrino detection experiment now aimed to study 330 kg of ^{136}Xe.

1.4.4 Tracker-calorimeter experiments

The use of heterogeneous detectors is rare in the field of $0\nu\beta\beta$ due to the need to develop several extra detector systems. In this category we classify the whole NEMO program which is profiting from combination of tracker and calorimeter (so-called tracko-calo method). They consist of three main parts: separate source of a studied isotope, tracker and calorimeter. Tracker surrounds the source material and its goal is to extract information about the trajectories of passing particles. Information about topology of each decay or other activity that takes places in the detector leads to much better background rejection. Calorimeter is used to measure particle energy which can be used to reject unwanted background activity as well. Important part of the NEMO program was NEMO-3 detector (Neutrino Ettore Majorana Observatory), which successfully measured $2\nu\beta\beta$ half-lives of 7 isotopes [29] (^{48}Ca, ^{82}Se, ^{96}Zr, ^{100}Mo, ^{116}Cd, ^{130}Te, ^{150}Nd). They used a thin source foil divided into sectors with different source isotopes to be able to measure all of them at the same time. A successor to NEMO-3, SuperNEMO [30], is currently under construction and is the one discussed in this thesis.

Chapter 2

SuperNEMO experiment

SuperNEMO is a heterogeneous detector searching for $0\nu\beta\beta$ of ^{82}Se. It is an improved version of the successful NEMO-3 detector. The demonstrator module of SuperNEMO project is placed in Modane underground laboratory (LSM) in France. All the detector systems of SuperNEMO demonstrator are already installed in laboratory and are currently taking commissioning data. In 2024, the shielding will be delivered and the demonstrator should be ready to take physics data. Let us have a look at the main detector systems of SuperNEMO demonstrator in more detail.

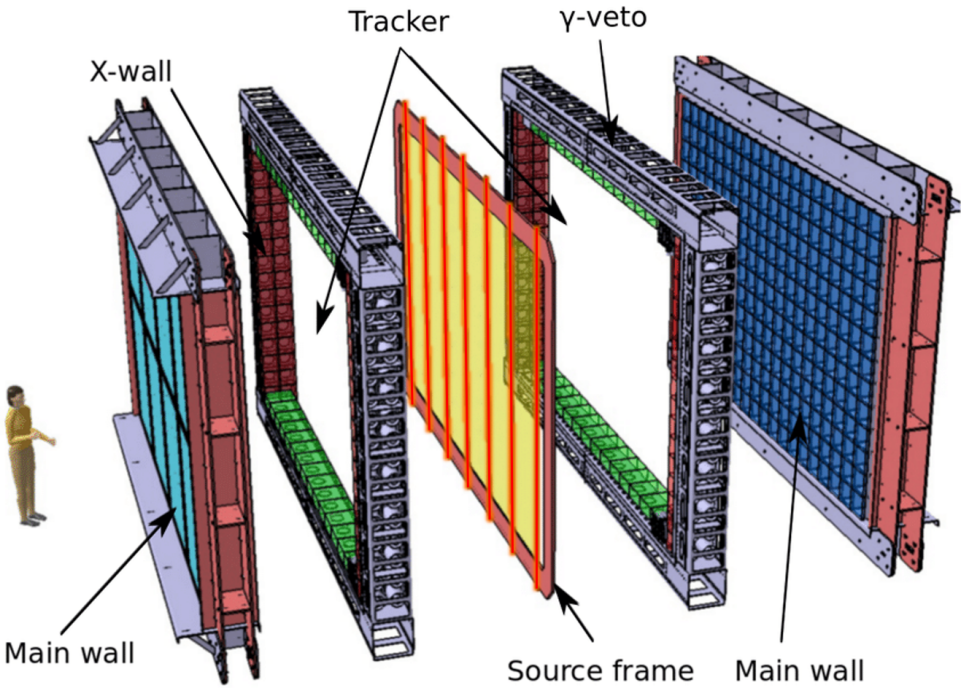

Figure 2.1: Overview of SuperNEMO demonstrator. Courtesy of SuperNEMO collaboration.

The coordinate system (x, y, z) with origin located at the centre of the detector is used by the collaboration and can be seen in Figure 2.2a. x axis is perpendicular to the ^{82}Se source foil and z axis is vertical. This convention will be strictly followed, throughout the whole thesis.

Because of the mirror symmetry of the detector along the source foil we divide entire detector into two sides. We call these sides Italian side and French side because the source foil is oriented and placed approximately coincidentally with the Italian French border.

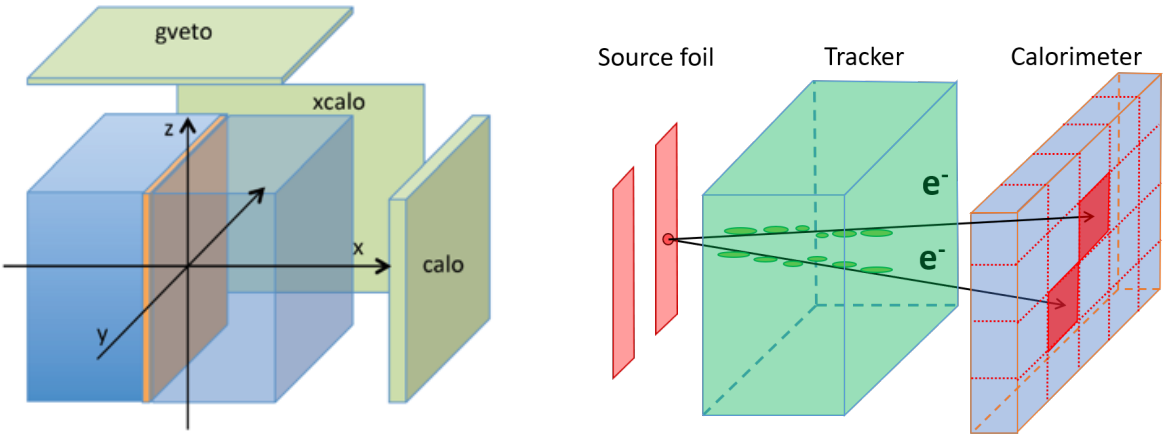

(a) SuperNEMO coordinate system

(b) principle of DBD detection

Figure 2.2: Plot (a) shows a schematic view of SuperNEMO with used system of coordinates. Orange plank in the middle represent source foil. Courtesy of SuperNEMO collaboration. Plot (b) shows the principle of DBD detection used by SuperNEMO demonstrator. The tracker measures the trajectories of the electrons emitted from the source foil. The electrons are then absorbed by the calorimeter which measures their energy. Courtesy of Vladyslav Yankovskyi.

2.1 Source foil

SuperNEMO demonstrator is using a set of thin foils composed of 6.11 kg of ^{82}Se [31]. When an electron is emitted from the source foil, it is passing through the material of the source foil itself. In order to limit the energy losses and changes of the momentum direction, it is important that the source foil is as thin as possible. In SuperNEMO, ^{82}Se is ground to powder and formed into 0.3 mm thin strips with spaces between them to make room for calibration sources.

2.2 ^{207}Bi energy calibration system

Energy calibration system is installed in the centre of SuperNEMO. It is a grid of 42 point-like ^{207}Bi sources that can be deployed and removed from the detector (Figure 2.3c). SuperNEMO demonstrator needs to be gas tight so it is not possible to access the inside of the detector. The deployment and removal of the sources is, therefore, performed by automatic deployment system based on the stepper motors and operated remotely. Each source is a small droplet of ^{207}Bi captured in a copper case with precisely measured activity and position in the case (Figure 2.3a). ^{207}Bi is a good calibration source because it is a source of monoenergetic electrons in the energy range of around 450 - 1000 keV which are the most common energies of single electrons from the $0\nu\beta\beta$ of ^{82}Se (Q-value of 2997.9 keV). ^{207}Bi undergoes electron capture with subsequent emission of gammas. An internal conversion can occur converting the released gammas into the monoenergetic electrons. Most common energies of these electrons are 976 keV and 482 keV [32].

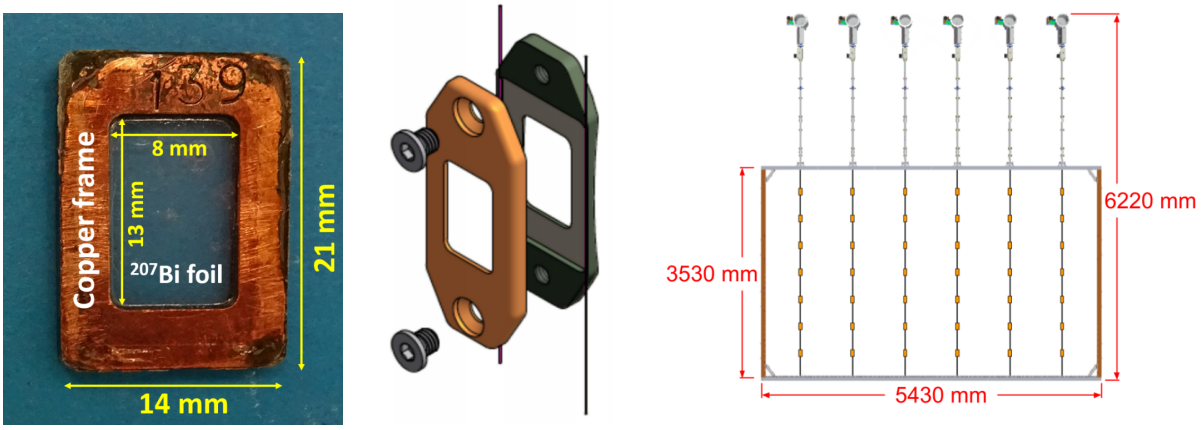

(a) (b) (c)

Figure 2.3: (a) Photo of a ^{207}Bi calibration source. The ^{207}Bi droplet is deposited in the center of the transparent mylar but it is not visible by naked eye. (b) Envelope used to mount the calibration source in the deployment system. (c) Schematic of the calibration system. Courtesy of SuperNEMO collaboration.

2.3 The tracking detector

What makes SuperNEMO stand out compared to other $0\nu\beta\beta$ detectors in its design is the ability to reconstruct the topology of an event (Figure 2.2b). This is possible thanks to the tracking detector (or "tracker"). It is a multiwire chamber composed of 2034 cells in Geiger mode (described in more detail in Section 3.1). A part of this grid of tracker cells can be seen in Figure 2.4. Goal of the tracker is to collect data about charged particles passing through its volume. Great advantage of this system is its great background rejection capabilities based on the event topology. With such sophisticated background rejection, the main source of background in SuperNEMO is predicted to be very rare $2\nu\beta\beta$.

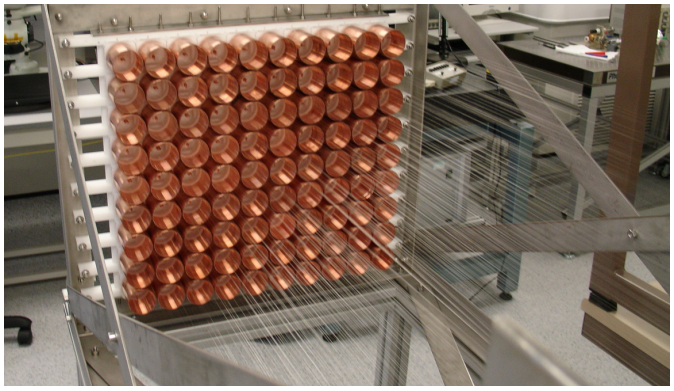

Figure 2.4: A group of 90 tracker cells during its assembly. Bottom cathode copper rings are visible as well as a grid of anode wires and field shaping wires. Courtesy of SuperNEMO collaboration.

The tracker is divided into Italian and French side. Both sides are 113×9 grids placed next to the source foil and calibration sources from Italian and French side respectively. Placement of the tracker cells is shown in Figure 2.5.

Volume of the tracker is filled with a mixture of Helium (95%), Ethanol (4%) and Argon (1%) [33]. Even in spite of great effort, because the tracking chamber is large and structured, it is not perfectly airtight and the gas leaks outside. Therefore, in order to keep the composition as stable as possible, this mixture is constantly being supplied to the detector to create overpressure inside the tracking chamber. Exact composition and pressure of the tracker gas plays a crucial role in tracker functionality and is carefully studied.

2.4 Segmented calorimeter system

The calorimeter system surrounds the volume of the detector from all six sides. It is composed of several segments, Italian and French mainwalls (Figure 2.6b) are the biggest segments and surround the detector from the sides parallel to the source foil. γ-veto surrounds the detector from the top and bottom and X-wall segments cover the smaller vertical sides perpendicular to the source foil (Figure 2.1). These segments consist of 712 individual parts in total, so-called Optical Modules (OM) which operate independently (Figure 2.6a). Each OM is composed of a scintillator block made of polystyrene (with addition of wavelength shifters pTP and POPOP [34]). When a particle enters the volume of the scintillator block, it deposits its energy in the block. The interaction of the particle with the block produces scintillation light. These photons are then collected by the photomultiplier tube (PMT) located in the back of the OM. PMT is then able to convert this microscopic energy signal from the deposited particle into the electric signal which can be read by installed electronics and digitized. The resolution is slightly differing between the OMs in the main wall. Nevertheless, according to the tests, the energy resolution of the best OMs are around 7.2% at 1 MeV [35].

2.5 Magnetic coil

SuperNEMO demonstrator dispose of a magnetic coil that is wined around the entire demonstrator. It is designed to produce 25 G of vertical magnetic field, homogeneous in the volume of the tracker. Presence of this field curves the tracks of charged particles. The curvature depends

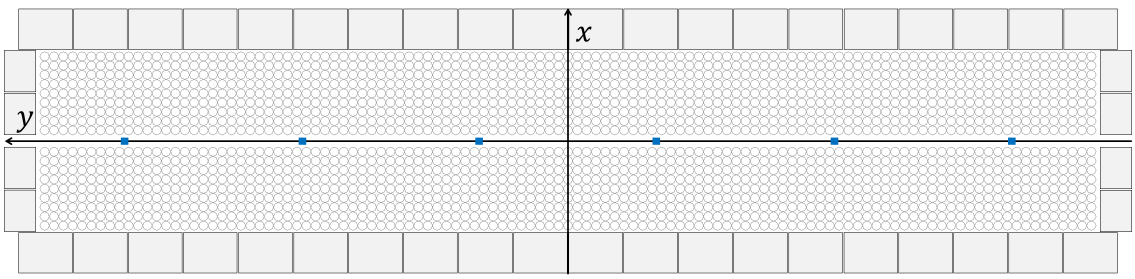

Figure 2.5: Schematic view of SuperNEMO in top projection. Black circles represent tracker cells, gray rectangles on the sides represent columns of OMs, small blue rectangles in the middle represent columns of calibration sources. The size of calibration sources is greatly exaggerated.

(a) optical module

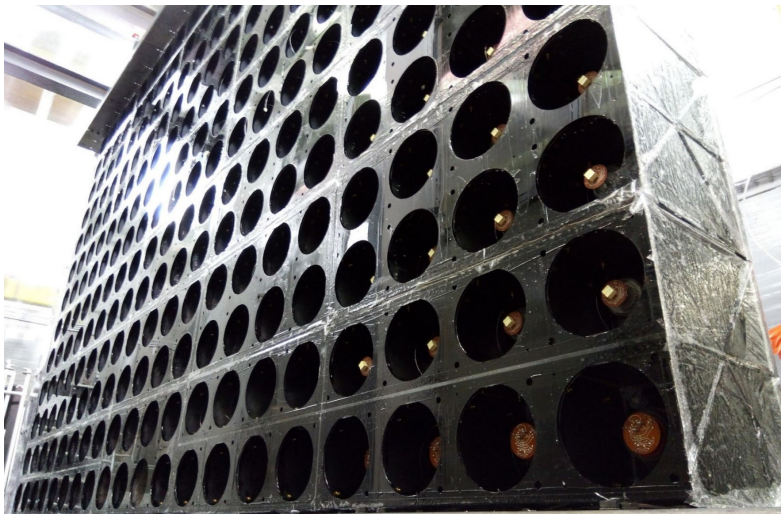

(b) calorimeter mainwall

Figure 2.6: Optical module (a) and calorimeter mainwall (b) as seen from the outside of the detector. Courtesy of SuperNEMO collaboration.

on the charge and the energy of the passing particle. This way, it is possible to distinguish between electrons and positrons for example, improving further the background rejection capabilities.

Experience with NEMO-3 has shown that it is difficult to ensure homogeneity of the magnetic field inside the detector. This fact complicates the reliability of the tracking. The tracks are not anymore perfectly circular and precise mapping of the magnetic field is needed. Due to this fact, the coil is currently installed but it was not yet turned on. Once the magnetic field would be turned on, some of the materials in the detector will get magnetized and the decision will not be reversible. More research on the effects of the magnetic field will be performed.

After a portion of the data will be registered without the magnetic field, the collaboration will reconsider the decision to leave the coil off. Nevertheless, all the data analyzed in the thesis were measured without the magnetic field.

2.6 Shielding and passive background suppression

Experiments searching for rare decays are particularly sensitive devices which need to be properly shielded. To block cosmic radiation that can reach the surface of the Earth, many of such particle detectors are built deep underground. In case of SuperNEMO, it is in the Modane underground laboratory (LSM) on the border between France and Italy. LSM is the deepest European underground laboratory and is located in the centre of Fréjus road tunnel. It is a tunnel under the Fréjus mountain connecting the two countries (Figure 2.7). This gives SuperNEMO a 4800 m.w.e. (meters of water equivalent) of shielding, corresponding to approximately 10^6 suppression of muon flux, which is equivalent to only around 4-5 muons per day and per m^2 [32].

For such sensitive device as SuperNEMO, the detector materials themselves can also act as a significant source of background – so-called internal background. It is important to choose suitable radiopure materials for the detector construction. Each material used for the construc-

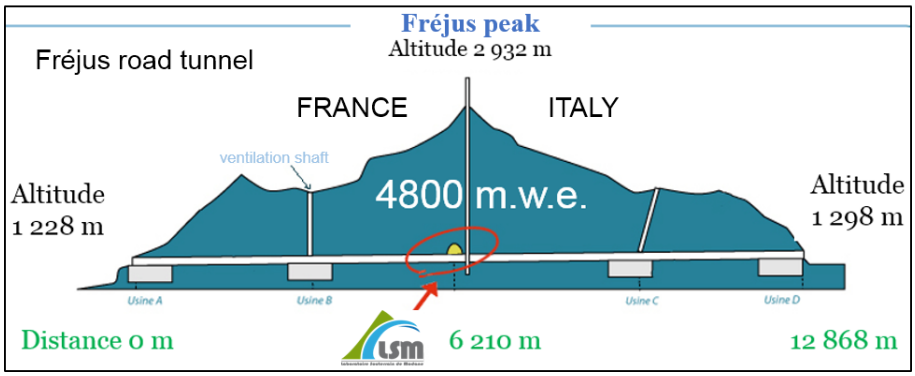

Figure 2.7: Fréjus road tunnel and location of LSM underground laboratory. Courtesy of SuperNEMO collaboration.

tion has to be carefully tested for the radiopurity. In case of SuperNEMO, a lot of effort was focused on impurities in the source foil. The contamination in the source foils is particularly dangerous because they can create DBD-like events with the vertices in the foils which are near to impossible to reject in the analysis. It was important to minimise the contents of ^{214}Bi and ^{208}Tl, which are main sources of background activity inside the source foils and the detector itself. The selenium needed to be enriched in order to maximize the amount of nuclei of the source isotope for a given volume of the foil. The collaboration managed to reach between 96% and 99.9% enrichment of the ^{82}Se source foil [33].

In underground laboratories it is typical to find a radioactive ^{222}Rn – an isotope originating from ^{238}U chain. This isotope has a half-life of approximately 3.8 days. To minimize the amount of ^{222}Rn in the atmosphere around the detector, an anti-Radon tent was installed around the detector. The tent is connected to air outlet leading to facility which cleans the air by capture of ^{222}Rn in activated charcoal. The clean air is after this process reintroduced into the tent.

To minimise the effects of all external background sources, a passive shielding is needed. In case of SuperNEMO, the shielding is currently in development. It is designed to have three layers. Outside layer is proposed to be made of iron. The middle layer will be built from polyethylene bricks filled with water. The final inside layer is already mentioned anti-Radon tent. All layers can be seen in Figure 2.8.

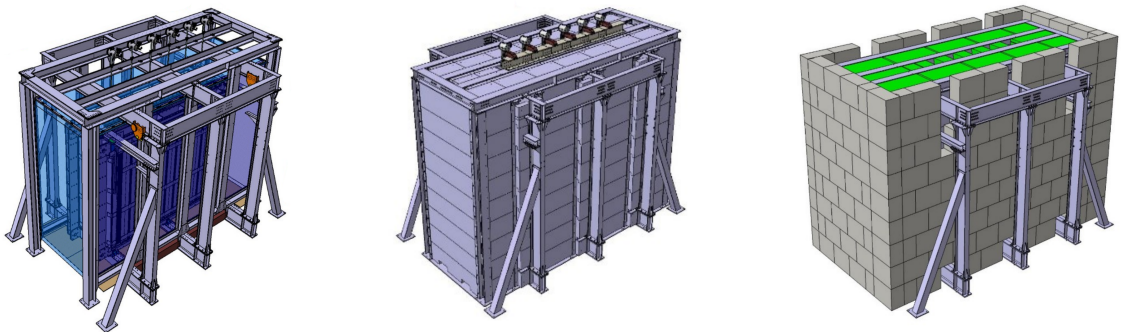

Figure 2.8: Layers of SuperNEMO shielding. Left picture shows the anti-radon tent, middle shows inner iron shielding and right one shows layer of shielding made of polyethylene bricks filled with water. Courtesy of SuperNEMO collaboration.

Chapter 3

Reconstruction of simulated data

3.1 SuperNEMO Geiger cell

As described above, the tracker consists of a grid of 2034 drift cells operating in Geiger mode. All tracker cells are about 3 m tall and 44 mm wide in both directions. At the top and bottom are placed cathode copper rings (top cathode and bottom cathode) and at the centre a thin anode wire under high voltage creating electric field. On the edge of each cell one can find twelve field shaping wires parallel to the anode wire. Each tracker cell has three vertical field shaping wires on each side and these are shared among neighbouring cells except for cells at the edge of the tracker system.

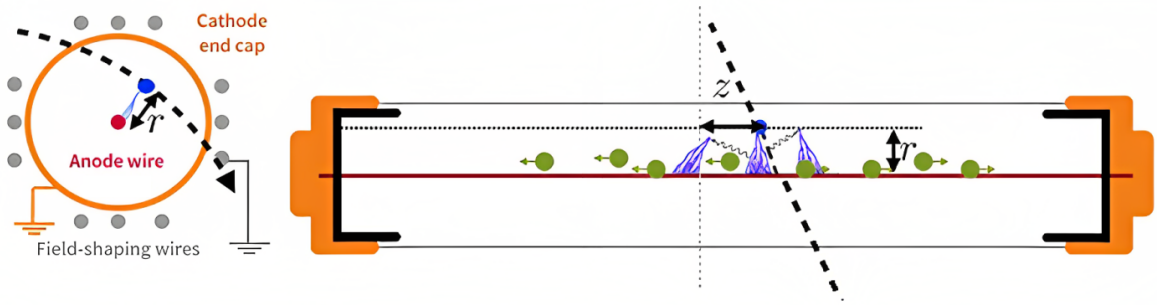

Figure 3.1: Top and side schematic view of SuperNEMO tracker cell. Black dashed line represents a passing particle, creating ionised particles (green). These can be used to reconstruct the height (z) and radius of the tracker hit (r). Courtesy of Cheryl Patrick.

When a charged particle crosses the volume of the tracker cell, it ionizes the gas – it tears electrons from the gas atoms. The electrons are then accelerated towards central anode and tearing more electrons from the gas atoms. This creates an avalanche which grows perpendicularly towards the anode (Figure 3.1). The avalanche is registered by the anode. The time it takes for the avalanche to develop (drift time) can be used to calculate the perpendicular distance r between the trajectory of a passing particle and the anode wire. This will be discussed in more detail in Sections 4.1 and 4.2.

The positively charged gas ions (plasma) produced in ionization are attracted by cathodes on the both ends of the cell. Part of the ions drifts towards top cathode and another part towards the bottom one. When the propagation reaches the cathodes, it influences the voltage on them which

is measured by electronics. Time difference between these two measurements is proportional to the height of tracker hit. Height corresponds to the z coordinate of the closest point to the anode wire on the particle trajectory (Figure 3.1).

3.2 Reconstruction of tracker data

When a tracker cell is triggered by a charged particle we refer to this occurrence as to a tracker hit (similarly for calorimeter hits). Each tracker hit is essentially a measurement of a particle trajectory. A single tracker cell, however, does not provide enough information to describe the entire trajectory. It only measures the distance of the closest point of the trajectory to the anode wire and the z-coordinate of the point. This is why an individual tracker hit is not represented by a point but a horizontal circle in the 3D space. If one obtains a signal from several tracker cells it is enough to fully reconstruct the track.

In order to reach SuperNEMO's full background rejection potential it is crucial to have a powerful reconstruction algorithm. The main goal of the thesis is to implement a first simple version of algorithm for linear track fitting based on the Legendre transform.

The question is what is the most efficient and reliable reconstruction algorithm. As explained above, the tracker data are equivalent to a set of horizontal circles in 3D space with different horizontal positions of centres x_i, y_i (positions of central anode wires), heights z_i and radii r_i. Throughout this work, we will identify tracker hits with their corresponding circles. When viewed from above, these circles should be tangent to the reconstructed trajectory (Figure 3.2).

Solution, we are looking for, is a trajectory that is tangent to all tracker hits. In the commissioning stage so far, SuperNEMO was measuring without the presence of magnetic field. It is, therefore, reasonable to expect that all particles in tracking volume follow a straight linear path. It is also possible to observe a path composed of several linear segments. Such situa-

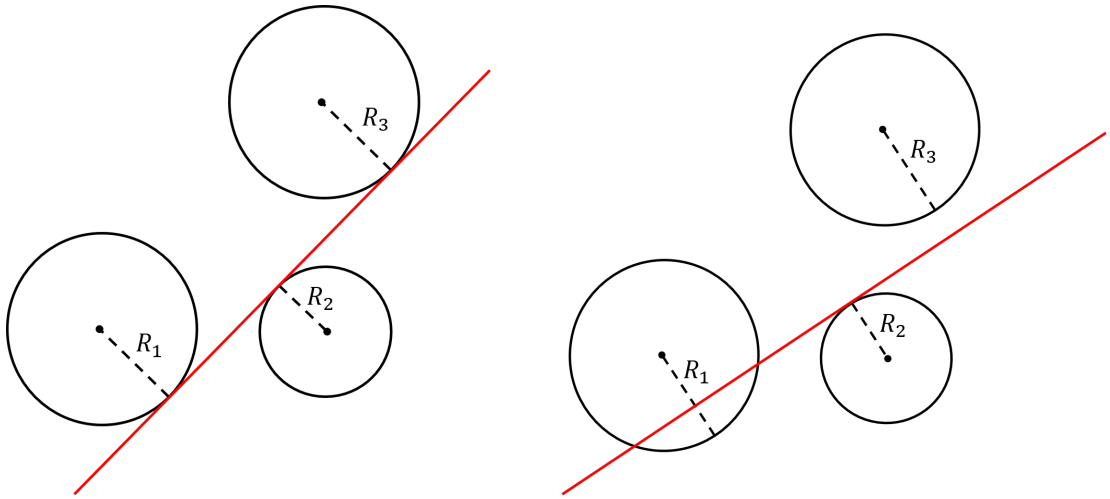

(a) good reconstruction (b) bad reconstruction

Figure 3.2: Comparison of two hypothetical reconstructed lines in the same demonstrative event viewed from above. Case (a) show a good reconstruction where the reconstructed line is tangent to all three tracker hits. Case (b) depicts a reconstructed line that is not tangent to the tracker hits, therefore, does not agree with measured values of radii.

tion happens when the passing particle occasionally interacts with another particle and changes suddenly its direction of travel. These direction changes are referred to as "kinks". The thesis is focusing on the linear tracks without kinks. The fitting of the tracks with kinks is, however, beyond the scope of this thesis and will be object of future research.

3.3 Reconstruction using Legendre transform

As discussed above, the mathematical solution to tracking problem in SuperNEMO is mathematically the same task as finding a tangent line to circles. This is only a part of the whole reconstruction, as it has to be done in all three dimensions. Nevertheless, the fitting in horizontal plane poses the most difficult part of the problem. In the vertical z-direction, we have precise information about the position, the tracker hit height z_i. This means, that we know exactly the z coordinate of the particle when it was the closest to the anode wire. However, in the horizontal plane, for each tracker hit, we have a set of all possible points that the particle could have crossed, corresponding to circles. This is what makes this part of the problem so difficult and why it requires much more attention than the vertical part of the reconstruction. To simplify the problem, we can split the reconstruction into two separate tasks. First, we will solve the reconstruction in the horizontal plane and then, we will reconstruct the vertical component of the track using the method of the least squares. For these reasons, only the horizontal part will be discussed in this chapter.

At the moment, the SuperNEMO collaboration dispose of a working reconstruction algorithm (CAT - Cellular automaton tracking). It is a NEMO-3 legacy code. This algorithm first clusters the tracker hits into groups based on their proximity to each other. Then, for all pairs of neighbouring tracker hits, it calculates all four of their common tangent segments. Finally, it tries to connect these short segments to form a longer path. This cellular approach provides some acceptable results, but it was mainly developed for the conditions with presence of magnetic field. Also, the code is no longer in a maintainable state to improve its reliability for the new experiment. The results are sometimes sub-optimal but it can still serve as a good benchmark, as an alternative method. Due to these facts, a new reconstruction technique has been proposed.

The new proposed technique is based on the Legendre transform. This transformation is widely used in thermodynamics and theoretical physics. It also has a useful geometrical interpretation that makes it promising for this type of trajectory reconstruction. This is because the Legendre transform of a function describes the original function in terms of its tangent lines. When applied to circles corresponding to tracker hits, it can provide us with a set of all tangent lines to those circles – the track reconstruction candidates.

The use and efficiency of this approach has already been demonstrated by T. Alexopulos et al. [36][37]. They used this technique for reconstruction of linear tracks tangent to elliptical tracker hits obtained from Monte Carlo simulations. In this chapter, we demonstrate the functionality of our own reconstruction software on idealized, simulated tracker hits. In the chapter 4, we will test its first version to the real SuperNEMO data.

3.4 Legendre transform of a circle

Let us first have a closer look at the Legendre transform. Let us have a function $y = f(x)$ that is defined, differentiable and convex on interval I. Function $y = f(x)$ defines a continuous curve – a set of points $(x, y(x))$. In each of these points, parametrised by x, we can find a tangential line $y = px - g$ (with parameters p, g) to the curve. Only certain combination of values of parameters p, g describe tangential lines to the curve $y = f(x)$. All these combinations can be expressed by a function $g(p)$. Legendre transform is a method how to obtain so-called Legendre image $g(p)$ of a function $y = f(x)$.

If the derivative $p(x) = f'(x)$ is reversible, we can find its inverse function $(f')^{-1}(p) = x(p)$, then Legendre image $g(p)$ of convex function $f(x)$ can be obtained by the following formula:

$$g(p) = x(p)p - f(x(p)) \tag{3.1}$$

The full derivation of this formula can be found in the Appendix A. Let us now apply this general transformation equation to a concrete example. Consider a circle with radius r and its centre at (x_0, y_0), given by equation

$$(x - x_0)^2 + (y - y_0)^2 = r^2. \tag{3.2}$$

In order to apply this transformation to this circle, we need to first divide the circle into its convex and concave semicircles. This allows us to describe the circle in Equation 3.2 with two explicit functions f_- and f_+:

$$f_\pm(x) = y_0 \pm \sqrt{r^2 - (x - x_0)^2}. \tag{3.3}$$

Now, we can apply the transformation from Equation 3.1 to both functions individually. We will start with the lower convex semicircle f_-. It is defined on interval $I = (x_0 - r, x_0 + r)$ and is differentiable and convex on I. Therefore, the conditions are valid and the transformation can

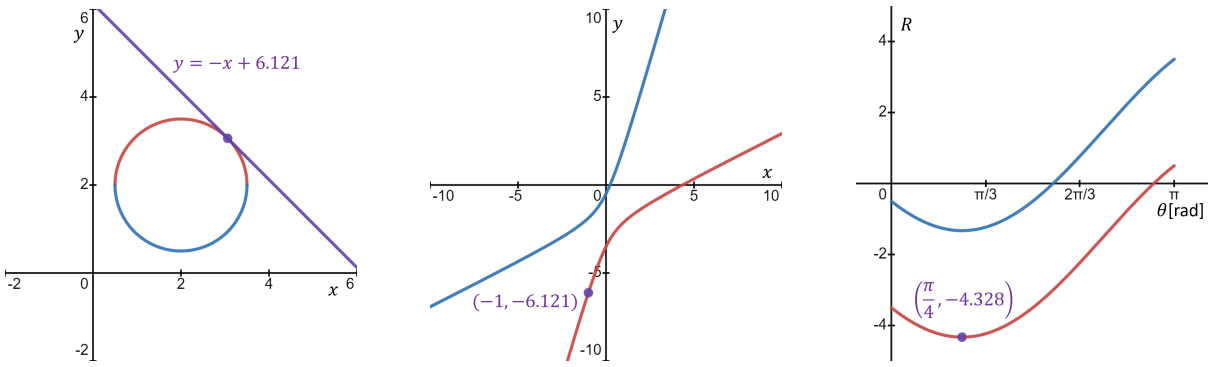

(a) circle and its tangent

(b) Legendre image of the circle

(c) Legendre image in (θ, R) space

Figure 3.3: Plot (a) shows an example of a circle with centre at $(2, 2)$, radius $r = 1.5$ and its tangent line with slope $p = -1$. Red function in the plot (b) corresponds to Legendre image of red upper semicircle in (a), similar for blue function in (b) and lower semicircle in (a). Highlighted point in plot (b) describes the tangent line in plot (a). Plot (c) shows the Legendre image in variables θ, R with highlighted point describing the tangent line. Plots were made using Desmos.

be used on this function. We can differentiate the function $f_-(x)$, and we obtain the function $p(x)$:

$$p(x) = \frac{\partial f_-}{\partial x} = \frac{(x - x_0)}{\sqrt{r^2 - (x - x_0)^2}} \tag{3.4}$$

Function $p(x)$ can be inverted, and we can express variable x as a function of p:

$$x(p) = x_0 + \frac{pr}{\sqrt{1 + p^2}}. \tag{3.5}$$

If we now plug $x(p)$ into Equation 3.1 we obtain the Legendre transform $g_-(p)$ of function $f_-(x)$ (Figure 3.3b):

$$g_-(p) = x_0 p - y_0 + r\sqrt{1 + p^2}. \tag{3.6}$$

Legendre transform of the upper concave semicircle can be obtained using the previous process which we used for convex functions. Let us define a function $f^* = -f_+$. This ensures that the function is convex and the transformation can be done using Equation 3.1 resulting in a following Legendre image:

$$g^*(p) = x_0 p + y_0 + r\sqrt{1 + p^2}. \tag{3.7}$$

This function describes all lines $y = px - g$ that are tangent to the function f^*. For its negative counterpart $f_+ = -f^*$, we have the same tangent lines but with parameters $-p, -g$ instead of p, g. In order to obtain Legendre image of the function f_+ we simply change the signs of p, g and obtain final following function:

$$g_+(p) = x_0 p - y_0 - r\sqrt{1 + p^2}. \tag{3.8}$$

Example of the image $g_+(p)$ can be seen in Figure 3.3a. Finally, the piecewise Legendre image of a given circle from Equation 3.2 is described by a following pair of functions:

$$g_\pm(p) = x_0 p - y_0 \mp r\sqrt{1 + p^2}. \tag{3.9}$$

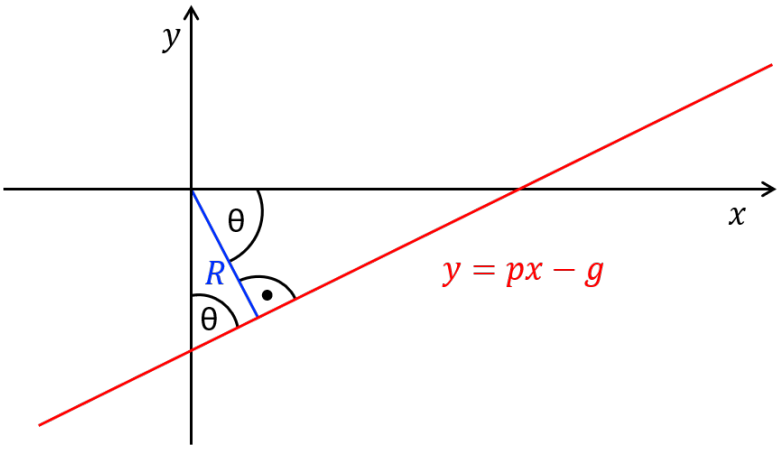

Figure 3.4: A line given by $y = px - g$ can be described using a different pair of parameters θ, R as seen in the picture.

3.5 Legendre image in (θ, R) space

Legendre transform in Equation 3.1 describes the tangent lines using slope p and an offset $-g$. As can be seen from Figure 3.4 one can parameterize the same line using two different parameters R and θ. θ is an angle between the line and vertical axis and R is an oriented distance of the line to the origin. This means, that the value of R can be positive as well as negative. At the same time, such definition, reduces the possible values of θ to interval $(0, \pi)$ while still preserving the uniqueness of description of each line.

This parametrisation is inspired by T. Alexopulos et al. [36]. The relationship between new parameters R, θ and old parameters p, g can be expressed in a following way:

$$g = \frac{R}{\sin\theta}, \qquad p = -\cot\theta = -\frac{\cos\theta}{\sin\theta}. \tag{3.10}$$

If we apply substitution in Equation 3.10 to the Legendre image of a circle from Equation 3.9 we obtain:

$$\frac{R_\pm}{\sin\theta} = -x_0\frac{\cos\theta}{\sin\theta} - y_0 \mp r\frac{1}{\sin\theta} \tag{3.11}$$

Finally, we can multiply both sides by $\sin\theta$ and get the final form:

$$R_\pm = -x_0\cos\theta - y_0\sin\theta \mp r. \tag{3.12}$$

For $\theta = 0$ the Equation 3.12 gains a form $R_\pm = -x_0 \mp r$, which is exactly what one would expect in case of vertical lines in Figure 3.5, except for the minus sign, which looks rather counter-intuitive. This is because of the definition of the parameter R. Similarly, we could use $\theta = \pi$ to describe vertical lines, which would result in the same value with a different sign. Both descriptions are equivalent, but we will use $\theta = 0$ and so we can generalize Equation 2.12 to interval $[0, \pi)$.

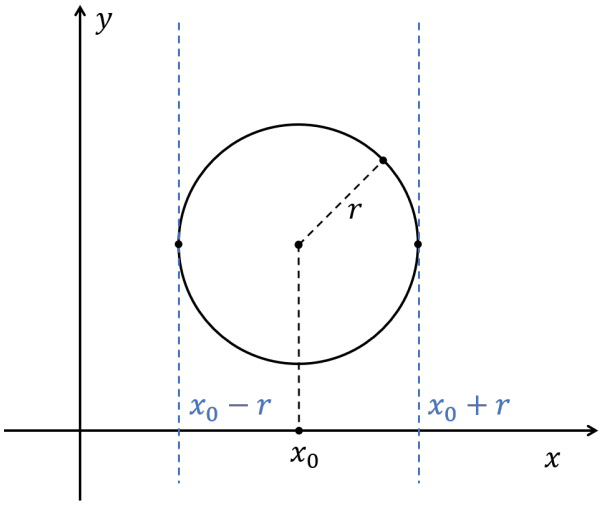

Figure 3.5: Example of a circle and its vertical tangent lines. Their distances to the origin are $x_0 - r$ and $x_0 + r$ resulting in a value of $R_\pm = -x_0 \mp r$ due to used convention.

Legendre image in the original variables p, g provides a unique description of all tangent lines to a given tracker hit, as shown in Figure 3.3. This means, that every point of the Legendre

image is a possible candidate for reconstruction, while the others do not fulfil the condition of tangentiality. However, the Legendre image in this form has a disadvantage. The domain of $g(p)$ (as well as its image) is the whole set of real numbers. This is very impractical for design of numerical algorithms which would search for fit candidates in $g(p)$. For the numerical algorithm we require that all tangent lines are described by a bounded set. This can be achieved by the substitution to variables θ, R.

Pair of sinusoid functions $R_{\pm} = -x_0 \cos\theta - y_0 \sin\theta \mp r$, where $\theta \in [0, \pi)$ uniquely describes all tangents to a given circle. The area containing all tangent lines is clearly bounded with respect to variable θ. In general, it is not the case for variable R. The transformation itself does not put any restrictions on value of R, but in reality it is limited by the physical dimensions of the detector itself. If we consider the origin of the coordinate system to be in the centre of the detector (Figure 2.2a), then any line that passes through the volume of the tracker should be at most about 2500 mm from this centre if we look on the top projection. Therefore, the value of R is practically limited to $[-2500\text{ mm}, 2500\text{ mm}]$ and so this substitution is convenient to design a numerical algorithm.

Last thing to be discussed, is how to use Legendre images of circles to reconstruct the common tangent line. Plot 3.6a shows three different circles and their common tangent line that we are searching for. Plot 3.6b shows Legendre images of the circles in (θ, R) space. These images have one point in common which describes a line, which is tangent to all three circles. The key principle of our reconstruction algorithm is, therefore, to search for this intersection of Legendre images. It corresponds to desired reconstruction candidate.

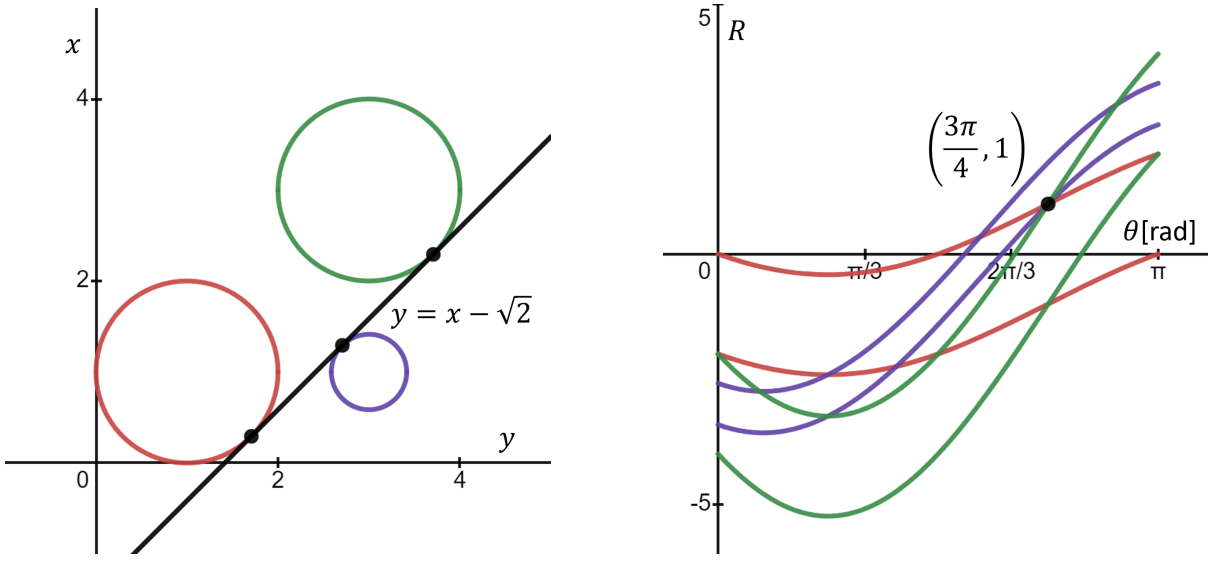

(a) Three circles and their common tangent line

(b) Legendre images of the circles

Figure 3.6: Plot (a) shows example of three circles with centres at $(1, 1)$, $(3, 1)$ and $(3, 3)$ and radii $r_1 = 1$, $r_2 = 1 - \sqrt{2}$ and $r_2 = 1$. Additionally, the plot (a) shows a common tangent line to the circles given by equation $y = x - \sqrt{2}$. Plot (b) shows the Legendre images of all three circles in (θ, R) space and a highlighted point $(3/4\pi, 1)$ describing the common tangent line.

3.6 Reconstruction of one-particle simulated data

Let us now demonstrate the performance of a tracking algorithm based on the technique described in the previous sections. For this purpose, the measured data from detector (referred to as real data throughout this work) are not suitable because they contain measurement errors. Therefore, to start with a simpler problem, we wrote a C++ code which produces perfect data originating from perfectly linear tracks (referred to as simulated data in this work).

As described in Chapter 2.3, the SuperNEMO tracker consists of two grids of tracker cells, one from each side of the source foil. Both of these grids are equidistant grids in both direction composed of 113 cells parallel to the source foil (113 rows) and 9 cells perpendicular to the source foil (9 layers) (Figure 2.5). The dimensions of our testing generator are not so important for the purpose of demonstration, nevertheless, we kept the grid structure of the tracker cells. We will consider each tracker cell as a square with sides of unit length and with an anode wire placed in its centre as can be seen in the Figure 3.7.

The generator should simulate data from a hypothetical tracker triggered by a passing particle moving on a straight linear path. The generator will accept the trajectory of a particle of our interest and should return a set of tracker data. As input we provide a line $y = ax + b$ described by two parameters a, b. And as an output the generator should give us a set of circles tangential to the line and with the centers at the center of the tracker cell crossed by the line.

For simulated tracker with a grid of $n \times m$ tracker cells,we calculate the simulated tracker data individually for each cell. In the first iteration, one tracker hit with index $i \in \{1, ..., nm\}$ is produced for each cell. The position of the centre is given by the position of its anode wire (x_i, y_i) in the centre of the cell. To calculate the radius r_i we simply calculate the distance of the

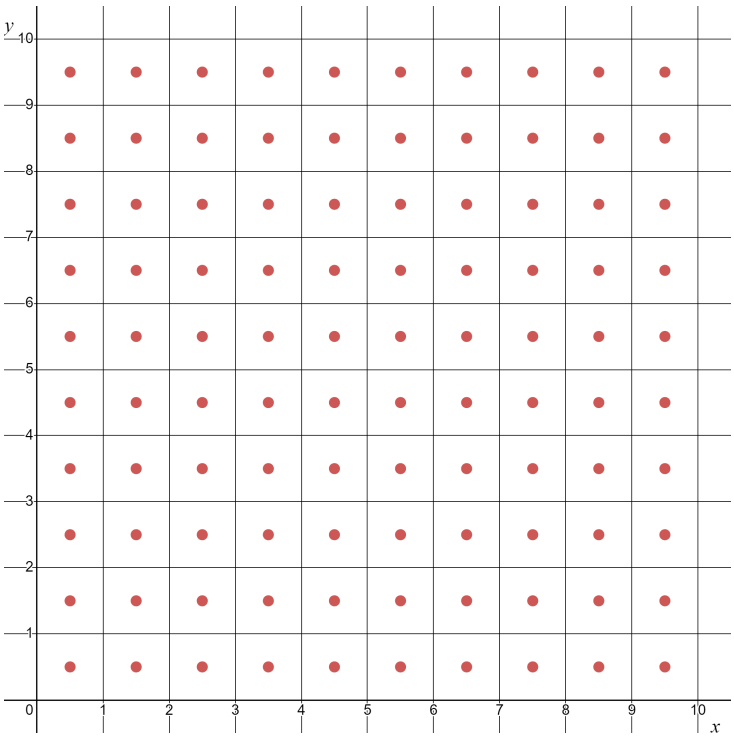

Figure 3.7: Example of a hypothetical grid of tracker cells. Red dots represent positions of anode wires. Plot was made in graphic calculator Desmos.

line $y = ax + b$ to the centre (x_i, y_i). We can do this using the following formula:

$$r_i = \frac{|y_i - ax_i - b|}{\sqrt{a^2 + 1}}. \tag{3.13}$$

In the second step, we have introduced one last limitation in correspondence to the real tracker. We do not expect a tracker cell to be triggered by a particle that has not crossed its volume. To mimic this behaviour, we only keep those tracker hits with a value of $r_i < \sqrt{2}/2$. In reality, this condition should depend on the direction of the line, however, presented simplification will be sufficient. We wrote this generator using C++ code and additionally used CERN library ROOT [38] for visualization. Plot in Figure 3.8a) shows example output from the generator. It represents a set of perfect tracker data (black circles) generated by a single line $y = -0.87x + 22.1$ passing through a grid of 25×25 tracker cells.

To reconstruct a simulated event by the generator, we apply Legendre transform and a substitution to (θ, R) space to all n circles. This provides us with a set of n pairs of sinusoid functions $R_{\pm}(\theta) = -x_0 \cos\theta - y_0 \sin\theta \mp r$. As demonstrated above, these pairs of sinusoid functions necessarily intersect in a single point, which correspond to the desired reconstructed track.

To find this intersection, we chose a numerical approach. We calculated functions $R_{\pm}$ for each tracker hit and plotted them in a 2D histogram (Figure 3.8b). Throughout this work, a plot depicting a collection of Legendre images of tracker hits will be called a sinogram. Use of a histogram limits our precision, but allows us to examine all $2n$ functions simultaneously. We can search the histogram in order to find its maximum. The maximum indicates the approximate

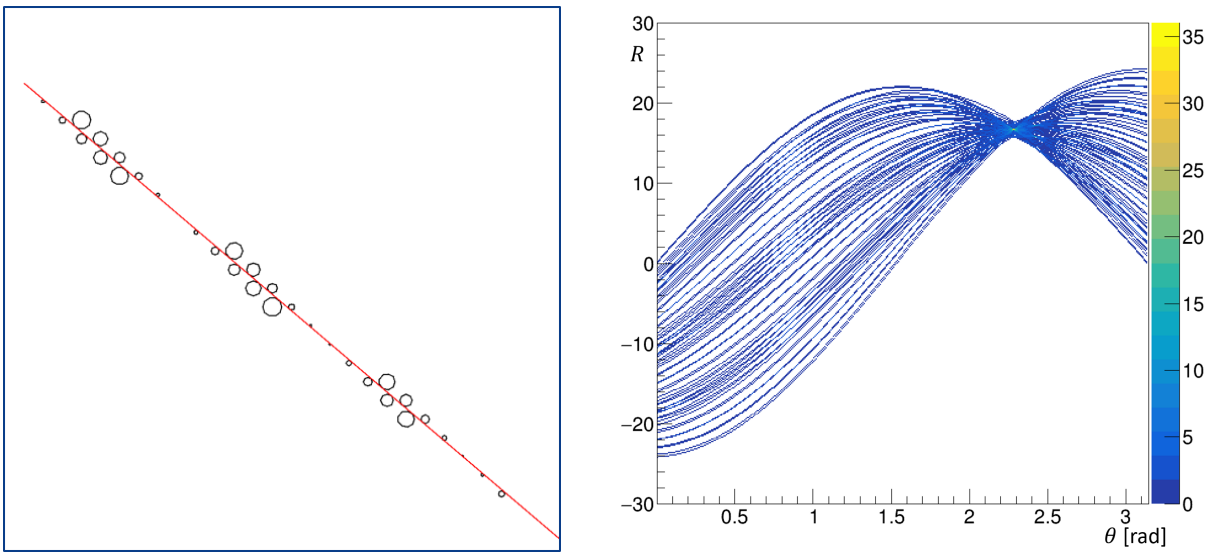

(a) Simulated tracker data

(b) Legendre image of the tracker hits

Figure 3.8: Plot (a) shows an example of simulated tracker data (black circles) generated by a line $y = -0.87x + 22.1$ using a grid of 25×25 tracker cells. The red line in plot (a) is a reconstructed track obtained from reconstruction algorithm. Plot (b) shows Legendre images of tracker hits in plot (a) plotted in a 2D histogram with 250×250 bins. A maximum is visible in approximately $(2.29, 16.6)$ indicating the position of the common intersection corresponding to the candidate reconstruction. Plots are made using ROOT library [38].

position of the most common point among these functions. This way we can find a candidate for reconstruction.

This approach has a very limited precision based on number of bins used in the histogram. The more bins we use, the more precise reconstruction we obtain, but at the same time, the computation time increases. To improve the precision, we can use an iterative search of the maximum. In each step, we find the position of the maximum and recalculate the plot for a smaller region centred around the maximum. In this way, we can achieve the desired level of precision. A demonstration of this iterative search is shown in Figure 3.9. Finally, after locating the position of the maximum of the histogram, we can use the transformation to the original coordinates (p, g). This allows us to compare the results with the input.

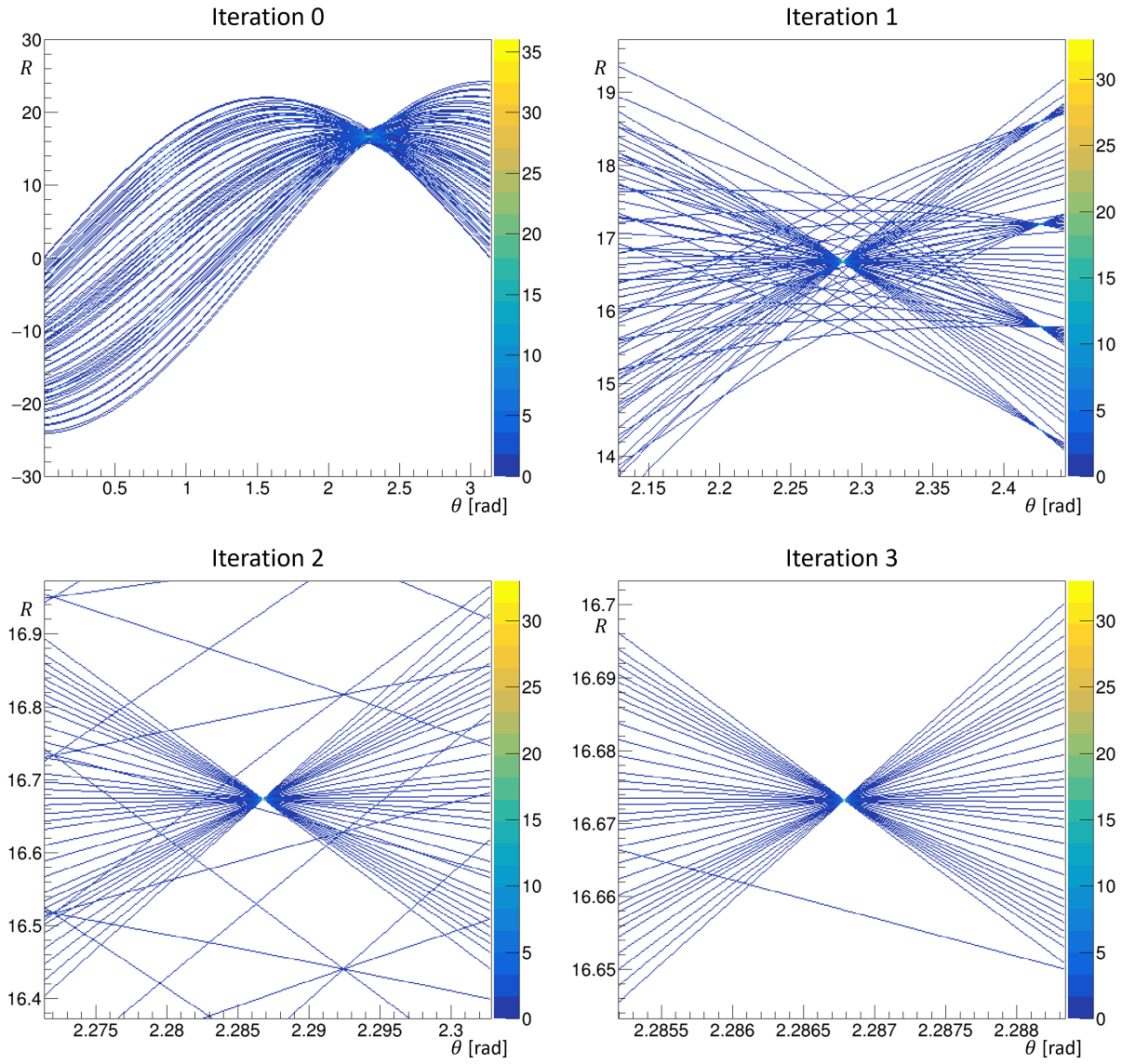

Figure 3.9: Example of 3-iteration search of a maximum of histogram originated from a line given by parameters $(p, g) = (-0.87, 22.1)$. The final reconstructed position is located in $(\theta, R) = (2.2867, 16.673)$ corresponding to values $(p, g) = (-0.870002, 22.0998)$.

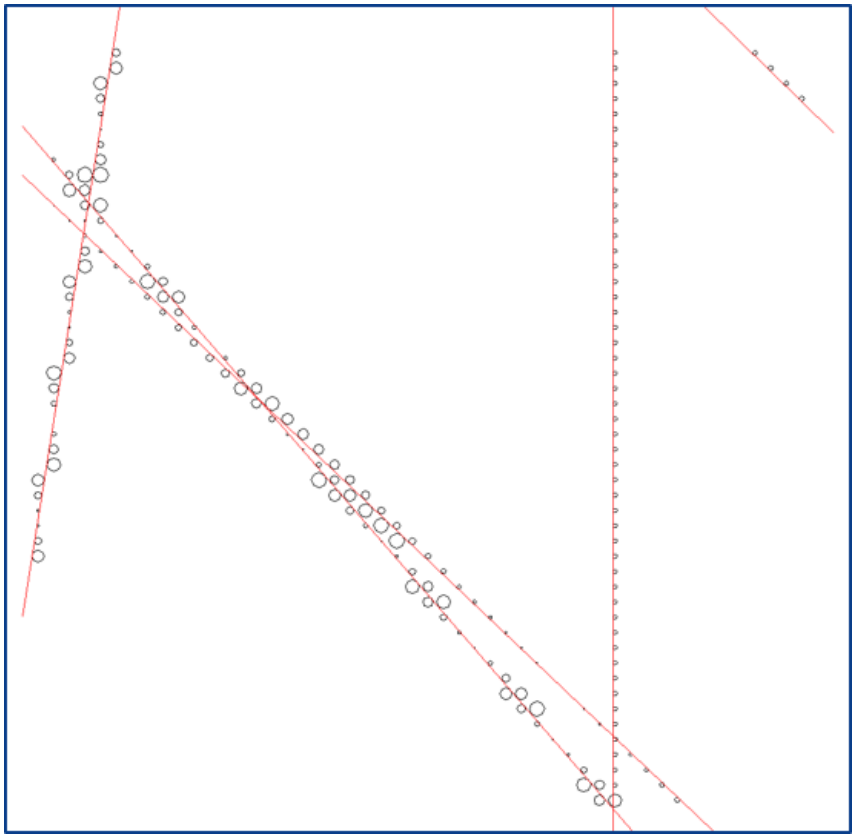

Figure 3.10: An example of simulated tracker data (black circles) generated by five different lines: $y = -x+95.2$, $y = -1.18x+43$, $y = -16328x+602000$, $y = 6.43x+18.5$, $y = -0.97x+40$. Five red lines correspond to obtained reconstructed tracks.

3.7 Reconstruction of multi-particle simulated data

Another thing that we are interested in is, whether the technique will be successful for more complicated events. For example, events with more than one passing particle. For this purpose, we need to improve the generator of simulated events to generate more particle tracks. This is only a small modification, however, it rises a question of what happens to the tracker data when more than one particle passes through a volume of a single tracker cell. In this case, we would need two different radii, one for each of two different lines. In reality, tracker cells undergo so-called dead time. This is a short period of time during which the cell becomes temporarily insensitive. The effect happens after a tracker cell has been triggered by a passing particle. During this period, the second particle arriving during the dead time window, is ignored. In the context of our generator this means that we will only keep data obtained from the first particle that we simulated. Example of simulated tracker data obtained from five particle tracks can be seen in Figure 3.10.

To reconstruct events with more tracks as in Figure 3.10 we had to improve the designed algorithm. This improved algorithm works in several steps and in each step it finds one track candidate.

At the beginning of the multi-particle fitting, a global maximum of the sinogram is found, following the iterative algorithm from Section 3.6. This produces a track candidate. Subsequently, the distance between each tracker hit and the track candidate is calculated. If the

distance is less than a certain threshold, we can consider these tracker hits to be associated to this track. We remove these tracker hits from the sinogram. After this process, we are left with a track candidate and a part of tracker data that probably did not originate from this track. Such remaining sinogram still contains several local maxima, representing several potential tracks. In the next step we repeat the process on the Legendre images of the remaining data. Figure 3.11 depicts sinograms obtained in different steps of such process.

With each step we obtain one more track candidate until we either have no tracker hits left to reconstruct or we have reached a certain limit of candidates that we want. An example of a successful reconstruction can be seen in Figure 3.10, where all five lines are successfully reconstructed.

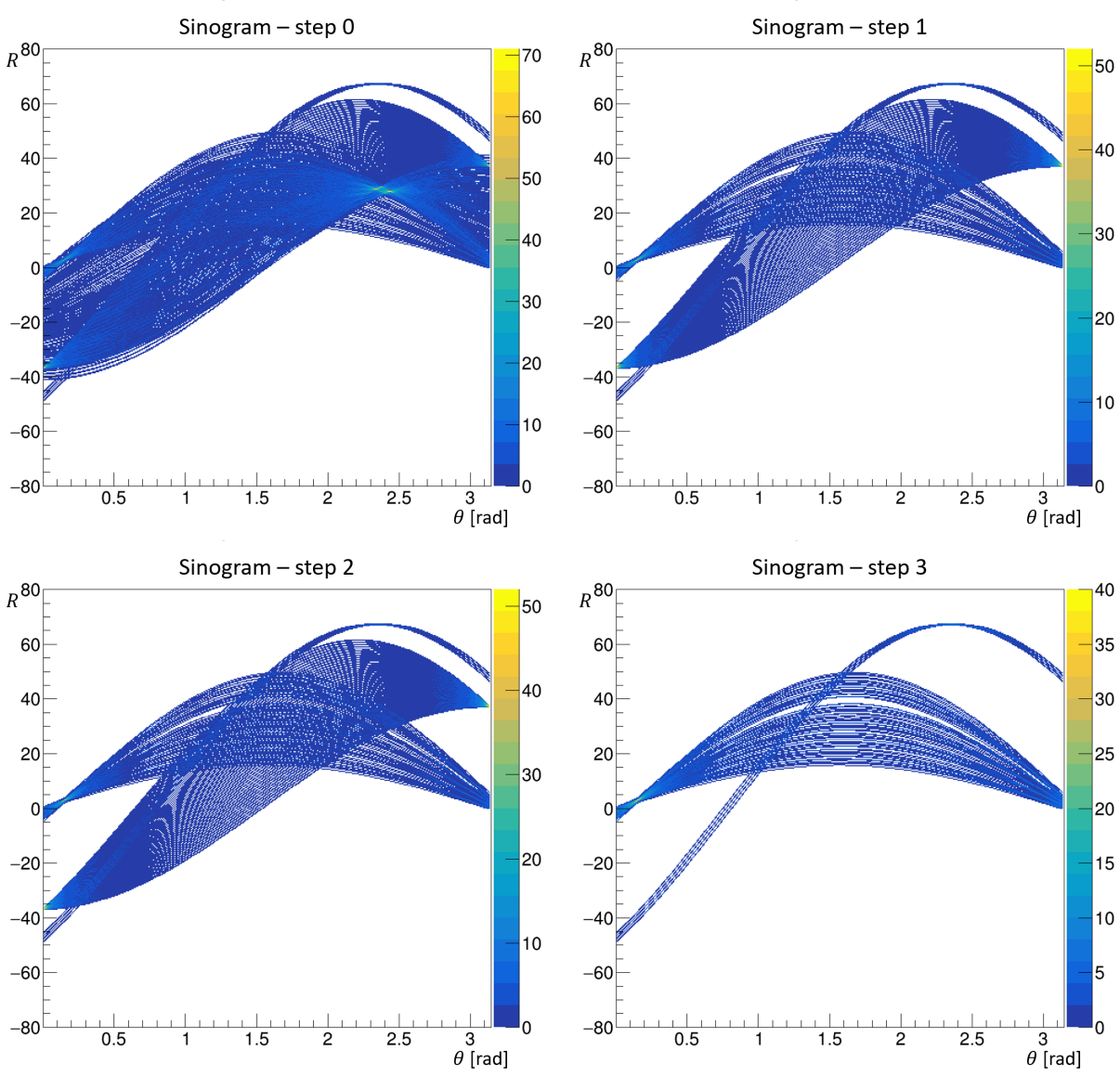

Figure 3.11: Plot of step 0 shows the original histogram with Legendre images of all tracker hits. In plots of next steps all tracker hits associated to a line found in the previous step were removed from the remaining tracker data.

Chapter 4

Reconstruction of real SuperNEMO data

In the previous chapter, it was demonstrated that the concept of Legendre images is working well for the simulated data without measurement errors. In this chapter, the main goal is to apply this approach to the real SuperNEMO data and analyze the potential improvements originating from the imperfect nature of the real data.

4.1 SuperNEMO data

To reconstruct the real SuperNEMO data we only need the values of tracker hit radii r_i and heights z_i, similar to Chapter 3. However, these values are not measured directly and are not available in raw SuperNEMO dataset. To obtain these values, we first need to describe the raw data in more detail.

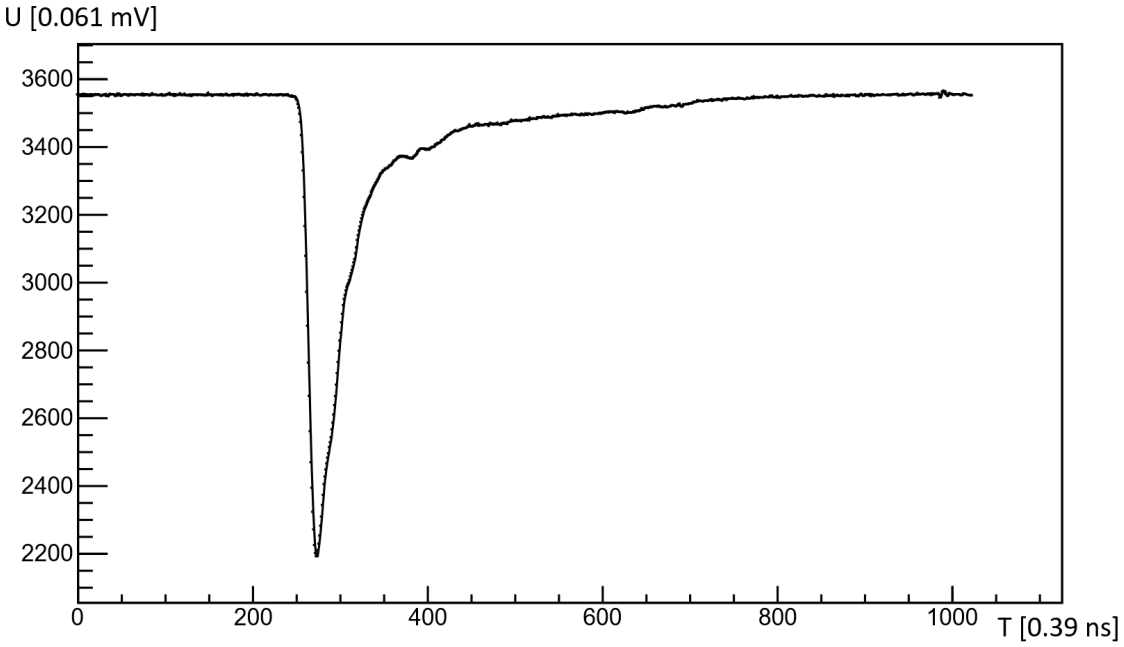

Figure 4.1: Example of a waveform obtained from OM.

The raw data from the demonstrator are organized into dedicated runs, identifiable by their unique numbers. These runs have different purposes and characteristics. In our work we were profiting from runs number 728 and 763. These runs were recorded with the ^{207}Bi calibration sources deployed in the detector. The sources emit a lot of electrons. The positions of all 42 sources are known with precision of few millimeters. This allows us to compare the position of the start of the reconstructed track with the positions of the calibration sources. This gives us the possibility to cross-check the success of the reconstruction. However, at that time the tracker was not fully functional and so run number 728 is recorded with only the first third of the tracker running and only the first two out of six columns of calibration sources deployed. Similarly, run number 763 had the second third of the tracker running and the second two columns of calibration sources deployed.

Essentially, we have two different sets of values stored in the data. One set is values measured by the tracker (tracker hits) and a second set is the values measured by the calorimeter (optical module hits).

Figure 4.1 shows an example of a waveform measured by OM. When the signal drops under a certain threshold (specific for each run) the OM is triggered and OM hit is created. OM hits contain an identification number of that OM, a timestamp and several integer values. These values determine basic characteristics of the measured waveform, such as its amplitude and integrated charge which can be used for the purpose of energy measurement (after the calibration). In some runs, entire waveforms can be stored for more detailed analysis.

Typical signal obtained from anode and cathodes of a tracker cell is shown in Figures 4.2a and 4.2b. In contrast to a waveform obtained from OM, the waveforms from tracker cell are more complex. Their important changes of the signal are encoded by 7 timestamps $t_0, ..., t_6$ as shown in Figures 4.2a and 4.2b. Together with the 7 timestamps the tracker hit contains an identification number of a given cell. Similar to OM hits, a tracker hit is created when the anode signal drops under a certain threshold. Time of this initial drop is encoded by timestamp t_0.

As briefly described in Section 3.1, when a charged particle passes through the tracker cell, it ionises the gas inside it. The electrons are accelerated towards the central anode by the electric field it generates. The electrons ionise more gas atoms as they travel, creating an avalanche of ions. When this avalanche reaches the anode wire, it affects the voltage that is measured. This produces a specific signal changes described by timestamps $t_0, ..., t_4$. Timestamp t_0 describes the time the when the avalanche first reached the anode wire. Timestamps $t_1, ..., t_4$ describe the times when the avalanche reached the cathode caps, as it also develops parallel to the anode wire.

The positively charged particles created travel parallel to the anode wire to the cathode caps at the bottom and at the top. This process is called plasma propagation. It travels at a constant speed towards both caps and when this propagation reaches the cathodes, timestamps t_5 and t_6 are created, defining the times of arrival.

To calculate the tracker hit height z_i we only need the timestamps t_0, t_5 and t_6. Unfortunately, some of these values are often missing. In these cases we do not use such hits in the reconstruction. However, in some cases it is possible to replace the values t_5 and t_6 with some of the values $t_1, ..., t_4$ with certain modifications. This improvement has not been implemented yet and requires more detailed research. In the future, the redundancy in the information would be an opportunity to replace missing pieces of information.

The hit height z_i is proportional to the delay between the arrival of the plasma to the respective cathodes, i.e. to the difference $t_5 - t_6$ and can be calculated as follows

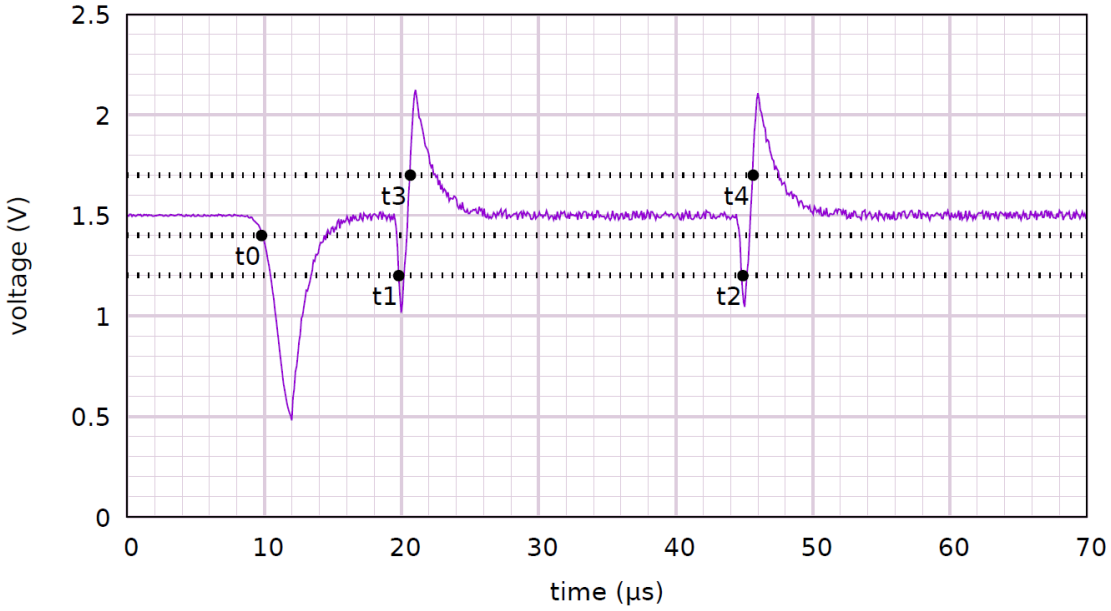

(a) Waveform from anode wire

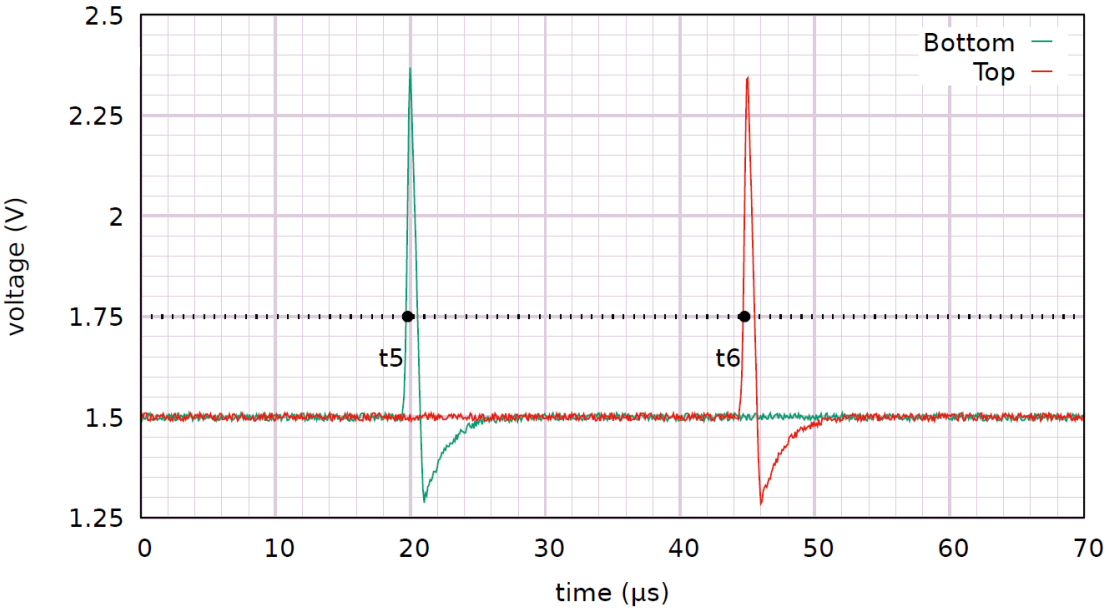

(b) Waveforms from cathodes

Figure 4.2: Plot (a) shows an example of a waveform from anode wire of tracker cell with highlighted timestamps $t_0, .., t_4$. Plot (b) shows examples of waveforms from cathodes of tracker cell with highlighted timestamps t_5 and t_6. Courtesy of SuperNEMO collaboration.

$$z_i = \frac{t_5 - t_6}{t_5 + t_6 - 2t_0} H - \frac{1}{2} H, \quad z_i \in [-1515\text{mm}, 1515\text{mm}] \tag{4.1}$$

where value $H = 3030$ mm is the height of the tracker cells.

Obtaining the value of hit radius r_i is even more complicated problem. It corresponds to the distance between the particle trajectory and the anode wire. It is based on measurement of so-called drift time (t_{drift}), which describes the time it takes for the ion avalanche to reach the

anode wire. The time of arrival of the ion avalanche to the anode wire is described by timestamp t_0, which is measured directly by the anode wire. If this timestamp is missing in the data, the radius cannot be calculated. For this reason, such tracker hits are classified as not suitable for reconstruction.

The time of the initial creation of the ion avalanche (referred to as t_{init}) is not measured directly. To obtain the value of t_{init} the calorimeter is required. Timestamp t_{init} corresponds to the time of the passage of a particle. To obtain this value, SuperNEMO takes advantage of the fact that the tracked charged particles are extremely fast. In case of $0\nu\beta\beta$ we expect the electrons to be relativistic, since Q-value of $0\nu\beta\beta$ is 2997.9 keV and the rest energy of the electron is approximately 511 keV. Similarly for electrons emitted from the calibration sources as described in Section 2.2. This means that these particles cross the entire volume of the tracker within a few nanoseconds at most. The avalanche, on the other hand, takes several microseconds to reach the anode wire. For this reason, the passage of a particle can be seen as instantaneous relative to the drift time. Therefore, the time the particle passed through the tracker cell (t_{init}) and the time it was absorbed by the calorimeter can be considered equal.

This means that the tracker data alone, without the OM hit, do not provide enough information about the tracker hits. This is one of the reasons why part of the calorimeter (mainwalls and X-walls) has a role of a trigger of the whole SuperNEMO demonstrator. Both tracker and calorimeter data are taken only when either mainwalls of X-walls (Figure 2.1) are triggered.

However, one problem arises from this technique. When more than one triggered OM in a single event is present, we do not know a priori in which OM was the charged particle absorbed. We developed two approaches for this association. The first associates a tracker hit to the nearest triggered OM. The second approach associates a tracker hit to the most recently triggered OM with respect to the tracker hit. Throughout this work, the distance based association has been used as it turned to be more reliable.

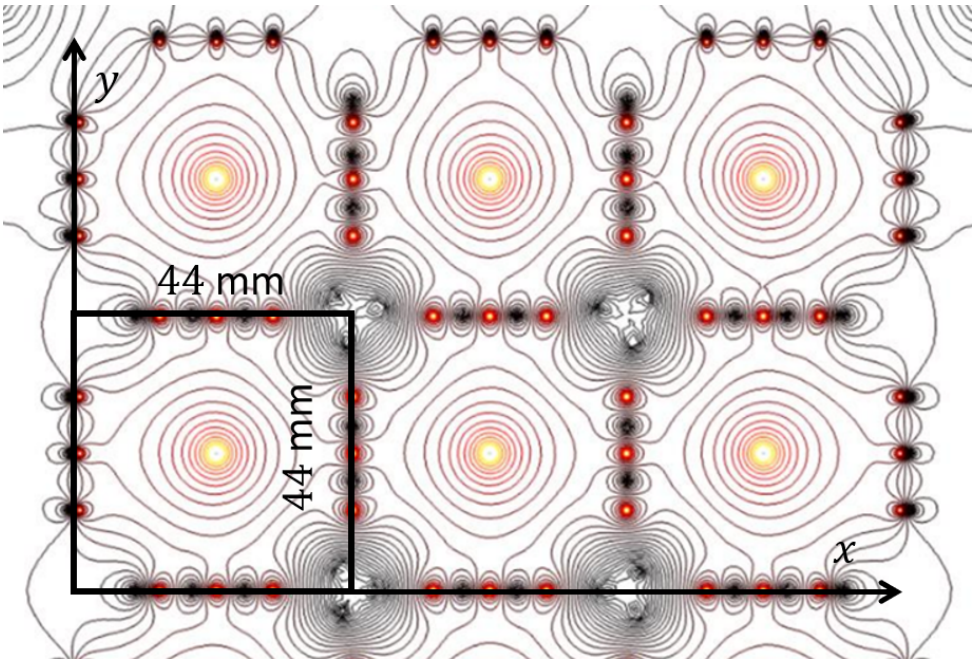

Figure 4.3: Simulation of electric field inside a set of six tracker cells as viewed from above. Courtesy of Cheryl Patrick.

4.2 Drift model

As described above, the distance r_i between the trajectory of the passing particle and the anode wire depends on the drift time ($t_{drift} = t_0 - t_{init}$). This dependence is described by so-called drift model. It can be obtained from simulations or direct experimental measurements and is currently being studied by the SuperNEMO collaboration. Two simplified models are already available.

Drift model depends on the electric field in the tracker cell, which generally has angular dependency. Shape of the electric field modeled in simulation can be seen in Figure 4.3. Simulations show that this dependency is negligible for distances up to approximately 2 cm from the anode wire, as can be seen in Figure 4.3. Therefore, the basic drift models available are simplified and do not reflect this dependency at all. This means that the drift models are a function of drift time t_{drift}. This ensures that the tracker hit from real data can be represented by circles. This simplification will not be possible with more complex drift model with angular dependence.

Figure 4.4 shows the two simple drift models, the red plotted drift model is extracted from the test which was performed with simple cell during construction of the tracker ("Manchester drift model"). The blue line represent a model extracted from from first simulations. In Figure 4.4 it is visible that both plots are piecewise functions. For values of radii up to about 22 mm (half-width of tracker cell) the functions behave very similarly. In this region they model the behaviour in the almost circular electric field. For values between 22 mm and $22\sqrt{2}$ mm the functions model behaviour in the corners of the tracker cells. For values greater than $22\sqrt{2}$ the function is simply an extrapolation and does not provide any meaningful results.

As already described, to obtain the value of the correct drift time, a tracker cell must be associated with OM hit that was triggered by the same particle. This is not always possible, the association can be unsuccessful, resulting in association of wrong OM hit to a given tracker hit. This can result in values of radius r_i greater than the dimension of the tracker cell, which should not be possible. This problem can be mostly solved by using the Manchester drift model, as it

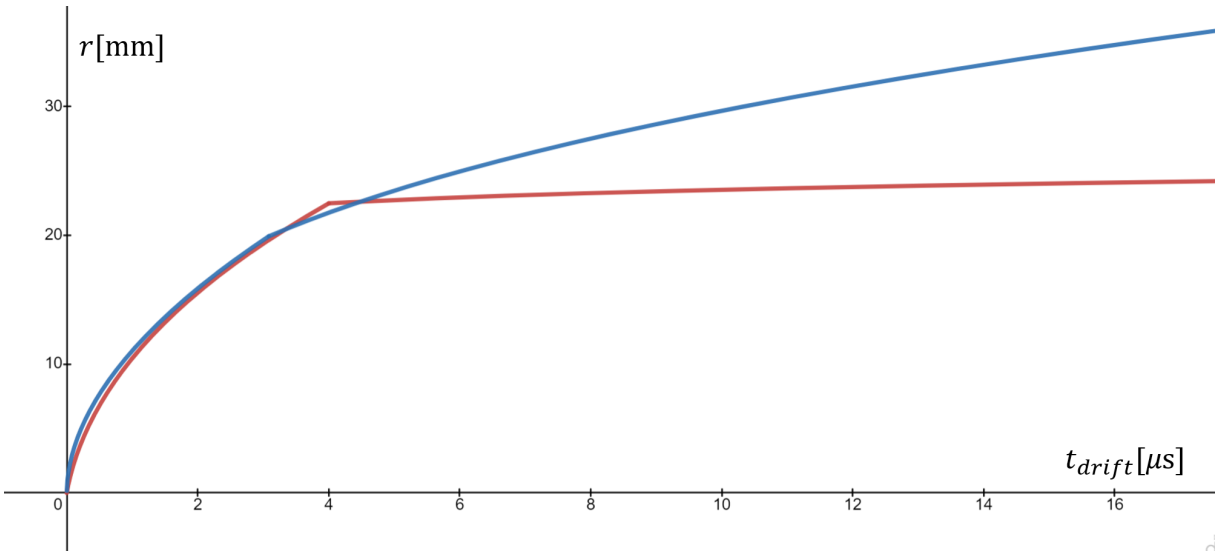

Figure 4.4: Two currently available simple drift models. The red plot corresponds to drift model obtained from experiments and the blue plot from simulations.

behaves almost as a constant function for distances above 22 mm. In some cases, this is still not sufficient and the obtained values of radius r_i are greater than a maximal possible distance of $22\sqrt{2}$ mm. Such tracker hits we tag as not suitable for reconstruction.

Finally, the drift model should describe the uncertainties of these values, since they come from a measurement with errors. These are important and must be taken into account when reconstructing an event. In the SuperNEMO collaboration some work on an advanced drift model with uncertainties has already been- done based on simulations, however, the model is still not in a suitable form for our purposes.

4.3 TKEvent library

As input data we used files in the RED (raw event data) data format. This data format groups tracker hits and optical module hits together into events. Ideally, these events should contain tracker hits and optical module hits triggered by a single process. In reality, these events represent several microseconds of all detector activity.

In order to work with real SuperNEMO RED data, it was necessary to first create tools that would allow us to perform the reconstruction. For this purpose, we wrote a C++ library called TKEvent [39] with a simpler data format containing only essential information for our work, and a converter from the original RED data format to our new format. Our data structure is similar to the RED data with additional modifications. Let us describe this data structure in more detail.

4.3.1 TKEvent

Class TKEvent is the main class and corresponds to events from RED data file. TKEvent contains its event number and run number, vectors of smaller classes, which correspond to tracker hits (TKtrhit) and optical module hits (TKOMhit) that belong to this event. In comparison to RED data format, we also included a vector of reconstructed tracks, described by a dedicated class TKtrack.

- ID number of the run
- ID number of the event
- vector of the OM hits
- vector of the tracker hits
- vector of the reconstructed tracks

4.3.2 TKOMhit

Each optical module hit is described by a TKOMhit object. This contains an identification number of this OM, a timestamp and a several integer values describing characteristics of the waveform signal. In addition, TKOMhit calculates and stores (x, y, z) positions of centres of these OMs.

- ID number of the OM
- x, y, z position of the centre of the OM in millimeters

4.3.3 TKtrhit

Each tracker hit is described by TKtrhit object which contains an identification number of a given tracker cell and 7 timestamps discussed in Section 4.1. TKtrhit stores calculated values of hit height z_i and hit radius r_i. In contrast to RED data format, TKtrhit also stores calculated (x, y) positions of corresponding anode wires (position of the centre of a given tracker cell in the horizontal plane).

As discussed above, an OM hit association is required in order to calculate hit radius r_i. This OM hit association is stored by objects of class TKtrhit. TKtrhit also contains associated reconstructed track if it is in a predefined proximity of this hit. In our work we used 6 mm as this limit. This is similar to the association of tracker hits to a track described in the section 3.7 used for reconstruction of simulated data. This allows us for better analysis and for better reconstruction of vertical component of the direction afterwards.

- ID number of the tracker cell
- x, y position of the anode wire in millimeters
- timestamps $t_0, ..., t_6$
- calculated hit height z_i in millimeters
- calculated hit radius r_i in millimeters
- associated OM hit
- associated reconstructed track

4.3.4 TKtrack

As mentioned above, the TKEvent library contains also class TKtrack. This class describes a track candidate by a set of four parameters (a, b, c, d), using a following description.

$$\begin{aligned} y &= ax + b \\ z &= cx + d \end{aligned} \tag{4.2}$$

This choice of this line parameterisation is based on the assumption that the reconstructed particle track is not parallel to the source foil. Such lines are of least interest and can be neglected. However, in the future the parametrisation of the line might be changed according to the needs of the final design of the tracking software. The TKtrack class also contains a vector of associated tracker hits. This association is mutual as seen above.

- side of tracker
- parameters a, b, c, d describing this line
- value of likelihood of this track
- vector of associated tracker hits

4.4 Data visualization

In order to browse the results of the track reconstruction in a more convenient way, we decided to write a visualisation script. Such visualisation is helpful for analysing the difficulties of the real data and the functionality of the reconstruction. We developed two types of visualization - two dimensional *xy* projection and full three dimensional scheme.

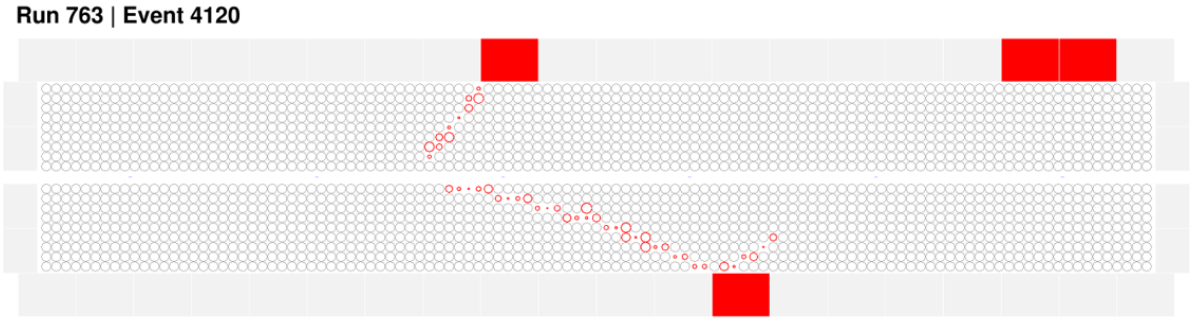

Figure 4.5: 2D visualization of event 4120 from run number 763.

We implemented the 2D simplified projection in the form of a dedicated function of TKEvent class (TKEvent::make_top_projection()). TKEvent::make_top_projection() generates a projection of a given event as seen from above and saves it as a picture. Example of this visualization can be seen in Figure 4.5. This visualization contains basic simplified geometry of several crucial detector parts. Namely, it includes all individual tracker cells marked by black circles, columns of optical modules marked by rectangles on the sides, and small calibration sources marked by small blue rectangles. These sources are visible only after zooming on them due to their small dimensions. Red rectangles in the visualization indicate triggered OMs and red circles indicate triggered tracker cells with their corresponding radii.

Full 3D visualization model is implemented with help of geometry classes (TGeoManager, TGeoVolume and TGLViewer) in CERN Root library [38]. The 3D model is fully interactive with possibility to zoom in and rotate each event. The 3D model incorporates the same crucial elements of the detector as the 2D projection, namely OMs, tracker cells and calibration sources. This feature is implemented in the TKEvent class as a function (TKEvent::build_event()) that builds the 3D geometry of the detector together with geometry of OM hits and tracker hits and saves them in a separate file. Additional script is then used to load and visualize this geometry. Examples of the 3D visualization can be seen in Figure 4.6a and Figure 4.6b.

4.5 Reconstruction of the real data

Having all the necessary tools for reconstruction and visualisation, we can finally attempt to reconstruct a real data event. In contrast to the reconstruction of simulated data in Chapter 3, real data are significantly harder to reconstruct due to several reasons.

Firstly, real data contain measurement errors in both values - the radius r_i and the height z_i. The uncertainty in height does not pose much problem as the vertical part of the problem is not that complex. However, uncertainties in radius can affect the quality of reconstruction a lot. The SuperNEMO tracker cells are supposed to provide substantially more precise data with smaller uncertainties than we are working with in this work. This is mainly because of the simple drift model that we used, as discussed in the Section 4.2. The drift model is not of its final design and introduces a lot of unnecessary errors in our data. New advanced model will provide more accuracy, however, it will make all calculations and algorithms of the reconstruction more complex.

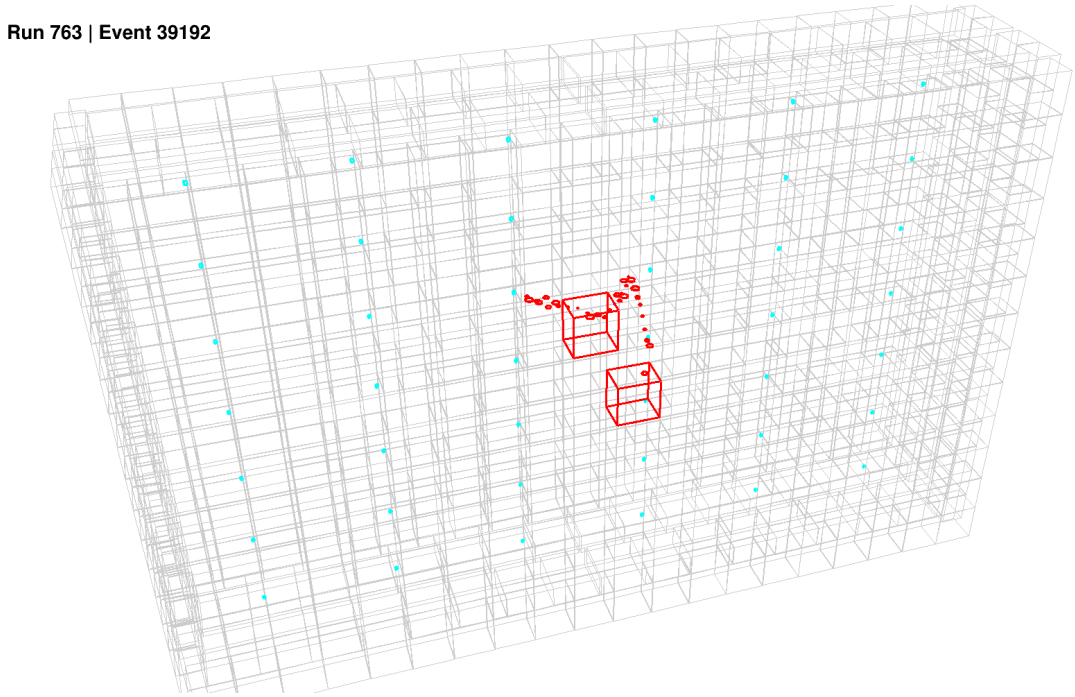

(a) overall view of the event

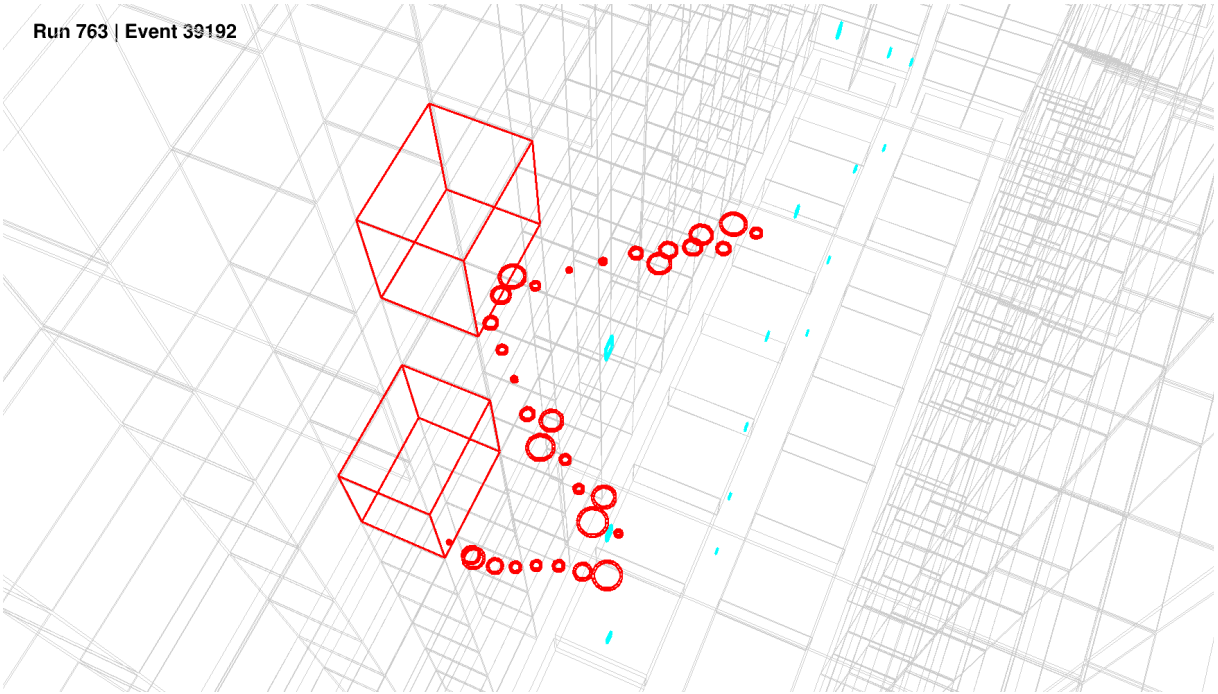

(b) more detailed view of the event

Figure 4.6: 2D and 3D visualization of real data event 39192 from run 763.

In Chapter 3, it was shown how to calculate Legendre images of each tracker hit. The intersection of such images corresponds to the reconstruction candidate(s). The complication which the "real world" measurement errors bring is demonstrated in Figure 4.7. In sinograms, the errors in hit radius are equivalent to a vertical shift of the Legendre images. Unfortunately, that means that a single intersection of the Legendre images does not exist anymore. Instead, we have to search for a group of intersections very close to each other. This limits the possible precision of reconstruction because we are not working with strictly consistent data.

Another difference to simulated data is a possible presence of noise in the data or the data which should be present but are missing (for example from the broken tracker cells). The track reconstruction algorithms which rely on the criterion of adjacency to decide whether a group of hits was initiated by one or more particles could have a problem with missing hits. This is also a case of current CAT reconstruction algorithm. Fortunately, this is where Legendre transform based reconstruction should be very robust because it searches for a collective characteristic of the tracker hits rather than local characteristics that would be disrupted by one missing hit or an additional one. Our proposed reconstruction algorithm searches for positions of maxima of the histogram containing Legendre images of tracker hits. If we have enough tracker hits in the event, the algorithm will result into sinograms with the same positions of maxima if one tracker hit is missing or if one additional is present in the data.

The tracker is divided by the selenium foil into Italian and French side. To simplify the reconstruction, the hits from each event were divided into two separate parts based on their side. Data from each side were reconstructed individually. This decision was made due to two main reasons. First reason is that we are mainly interested in particles emitted from the source foil between the two sides. Such particles do not cross from one side to another through the

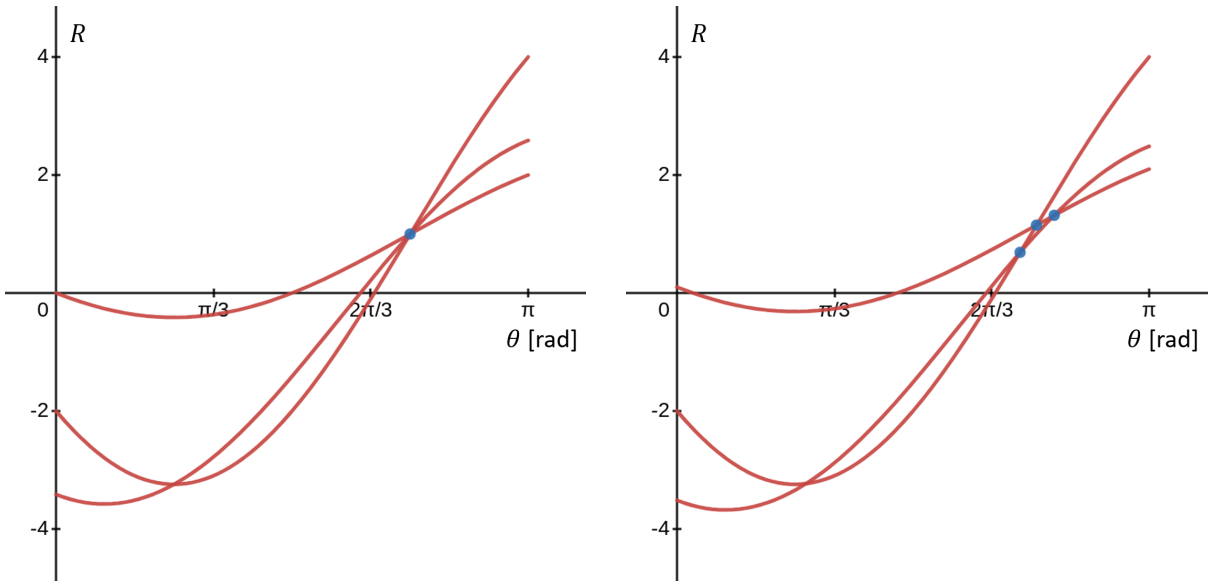

(a) Legendre image of precise data

(b) Legendre image of imprecise data

Figure 4.7: Demonstration of the effect of measurement errors in data. Plot (a) depicts Legendre images of three simulated mathematically accurate tracker hits. All three lines meet at a single point. Plot (b) depicts Legendre images of the same tracker hits with small added error in radius. The three lines do not have common intersection.

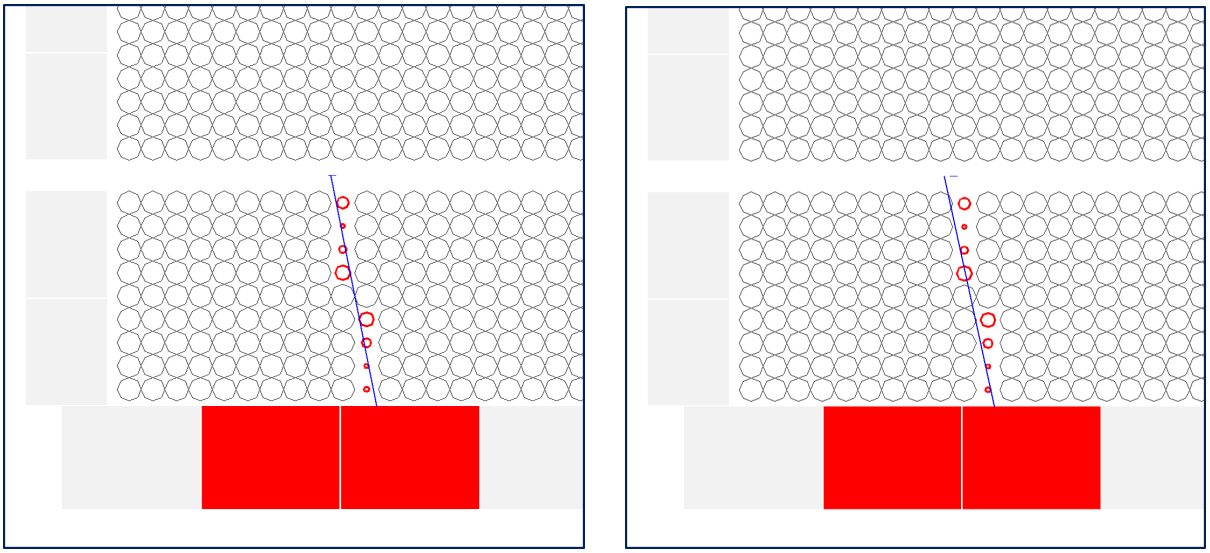

(a) reconstruction done using 2 iterations

(b) reconstruction done using 4 iterations

Figure 4.8: Comparison between reconstructions of event 7 in run 728. Plot (a) is done with only 2 iterations while plot (b) is done using 4 iterations.

source foil[1]. Second reason is that we can expect a change in direction when a particle passes through the source foil as the foil is much denser than the tracking gas. We can expect some particles with high energies (e.g. muons) to preserve their direction if they pass through foil but, in general, it is not the case.

To perform the reconstruction, we first filter tracker hits that are not suitable for reconstruction as described in Section 4.2. The tracking is meaningful only under a condition that we have at least three of these hits available on one side of the tracker. This is because a line is uniquely determined by minimum of three circles tangent to it. Then we calculate and plot Legendre images of tracker hits into a histogram. As discussed at the end of Section 3.5, reasonable region of the histogram is $(0, \pi) \times (-2500\text{ mm}, 2500\text{ mm})$ as this region contains representation of all possible lines crossing the tracker.

Finally, we can use the algorithm designed in Chapter 3 for iterative searching of the precise position of maximum in this histogram. However, as described and demonstrated in Figure 4.7, the common intersection does not exist in case of real data. If we zoom enough into the sinogram (with sufficiently small bins) the histogram will show these individual intersections as separate points. These intersections will be plotted in different bins compromising the key principle of this technique - the collection of intersections of more than two sinograms. This puts a limit on the achievable precision with this simple algorithm to the size of a bin that can reliably cover the area of most of the intersections.

In Figure 4.8 a comparison of reconstruction obtained from 2-iteration search with a reconstruction obtained from 4-iteration search is demonstrated. Each new iteration recalculates the histogram on area of only 10% of the previous size which means 10× increase in precision with each iteration. In the final iteration, position of a single bin is chosen. In this case, the histogram

[1]This is not true only in rare cases when the particle dramatically changes its direction during flight or bounce off the calorimeter wall back to the other side. Even in those cases, it does not pose a problem to separate these tracks into two.

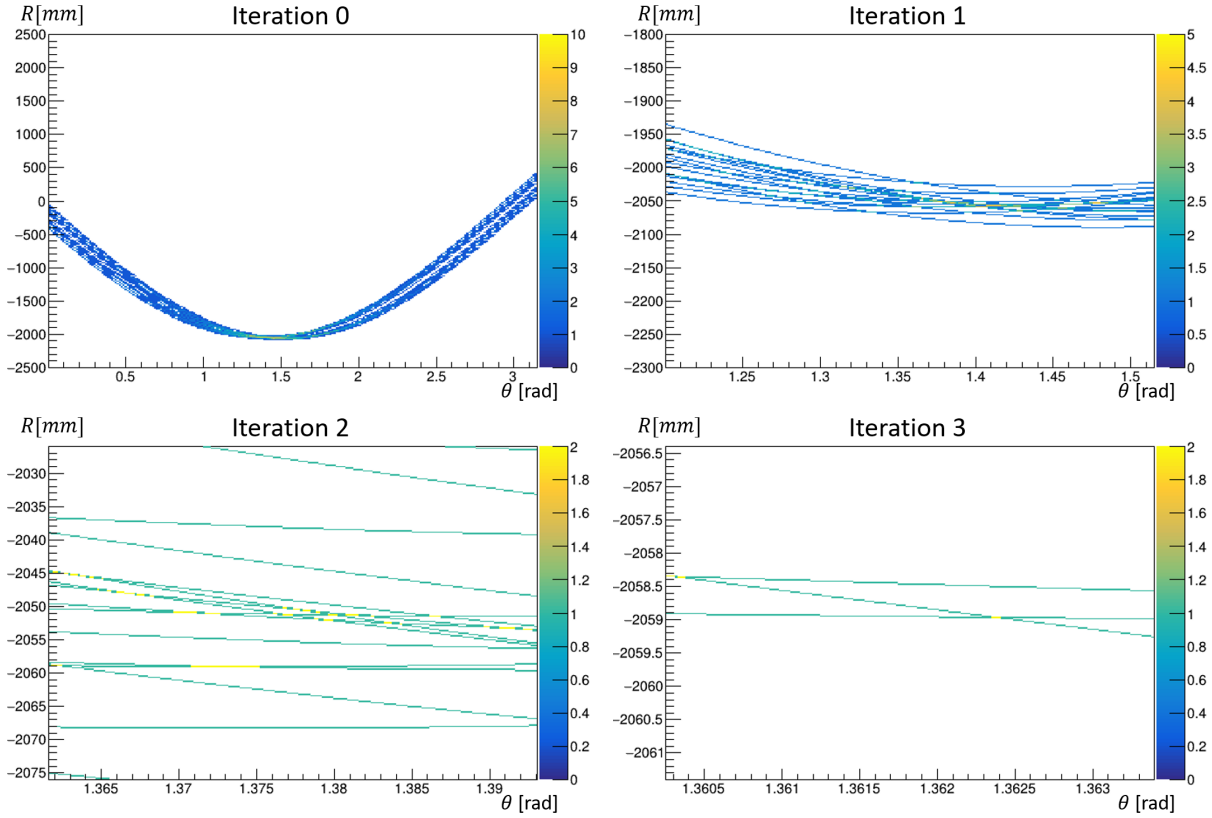

Figure 4.9: Sinograms in each iteration from reconstruction of event 7 in run 728.

is divided into 250×250 bins. This results into a final precision of 2 mm and about $1.3 \cdot 10^{-3}$ rad for the 2-iteration search and 0.02 mm and about $1.3 \cdot 10^{-5}$ rad for the 4-iteration search.

Sinograms of individual iterations from this event can be seen in Figure 4.9. In iteration 0, the global maximum of the histogram is 10, indicating that Legendre images of multiple tracker hits are present in this bin. With smaller bins in iteration 1, the maximum drops but still represents a unique global maximum. In iterations 2 and 3, the histograms contain multiple maxima with value 2 indicating crossings of individual pairs of Legendre images. This provides no reliable indication of the position we are interested in. Such behaviour is a result of uncertainties in the data. An extra improvement is needed.

4.6 Reconstruction by inclusion of Gaussian uncertainties

To overcome the problem described in previous section and to improve the precision of reconstruction Alexopulos et al. [36][37] implemented a Gaussian blur of the Legendre images of the hits. Our solution is very similar and introduces a step towards future implementation of uncertainties of drift model into the reconstruction.

When a particle passes near an anode wire, it uniquely determines a circle which represents a tracker hit from perfect detector. However, the real tracker measures with errors and so we expect the values of r_0 and z_0 to follow some distributions as shown in Figure 4.10.

These uncertainties of r_0 should be described by advanced drift model, however, such model is not available yet (as discussed in Section 4.2). For this reason, we decided to keep the simple

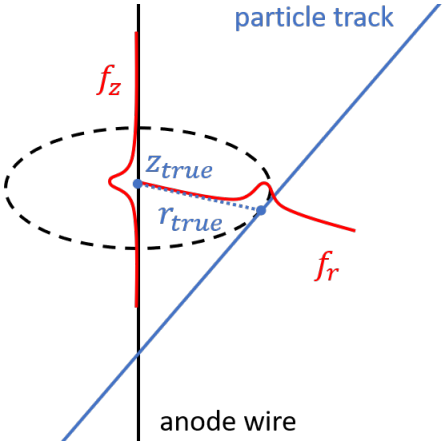

Figure 4.10: Measured value of radius r_0 is not equal to real theoretical value r_{true} but follows a distribution as demonstrated. Similarly for measurement of hit height z_0.

Manchester drift model as we used before and improve it with simpler artificial uncertainties. In order to implement the uncertainties we have chosen a Gauss distribution with $\sigma = 2$ mm. In reality, the uncertainties of radius r_0 are expected to be even smaller and dependent on the value of r_0. We consider them as independent for simplicity. Originally, a tracker hit was represented by a single value of r_i and a corresponding Legendre image $R_i(\theta)$. After the introduction of the uncertainties the radius is rather represented by a distribution of radii r. Each value of r has a different weight described by probability density function

$$f_i(r) = \frac{1}{\sqrt{2\pi}\sigma} \exp\left(-\frac{(r - r_i)^2}{2\sigma^2}\right). \tag{4.3}$$

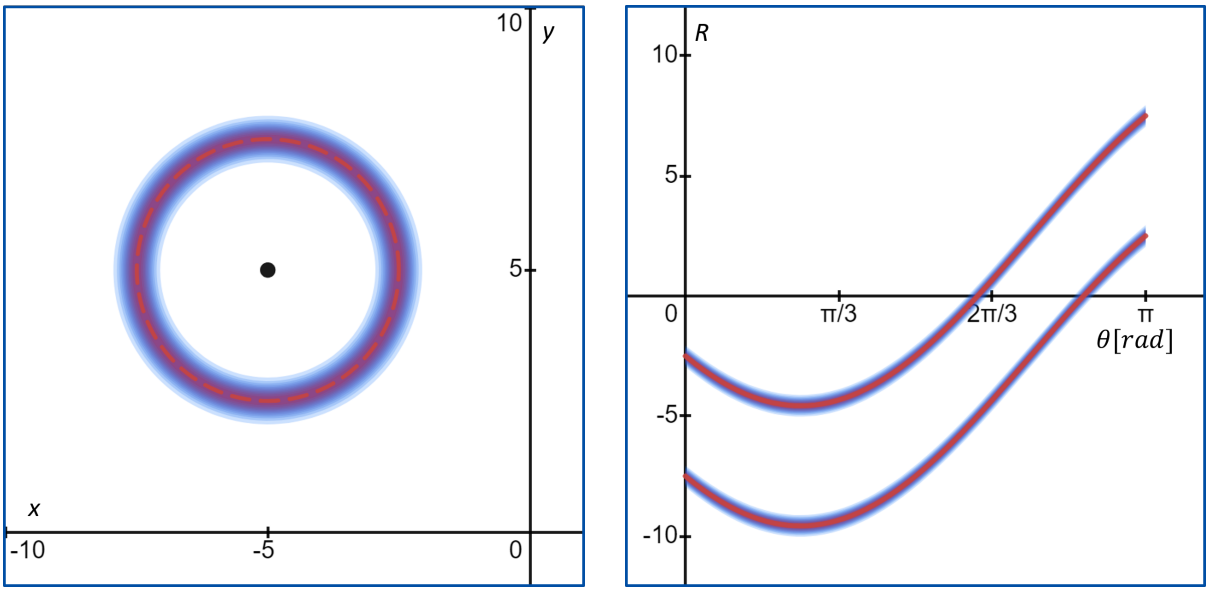

(a) tracker hit with uncertainties

(b) distribution of Legendre images

Figure 4.11: A demonstration of a tracker hit with its corresponding Gaussian uncertainties in plot (a) and a distribution of Legendre images of this hit.

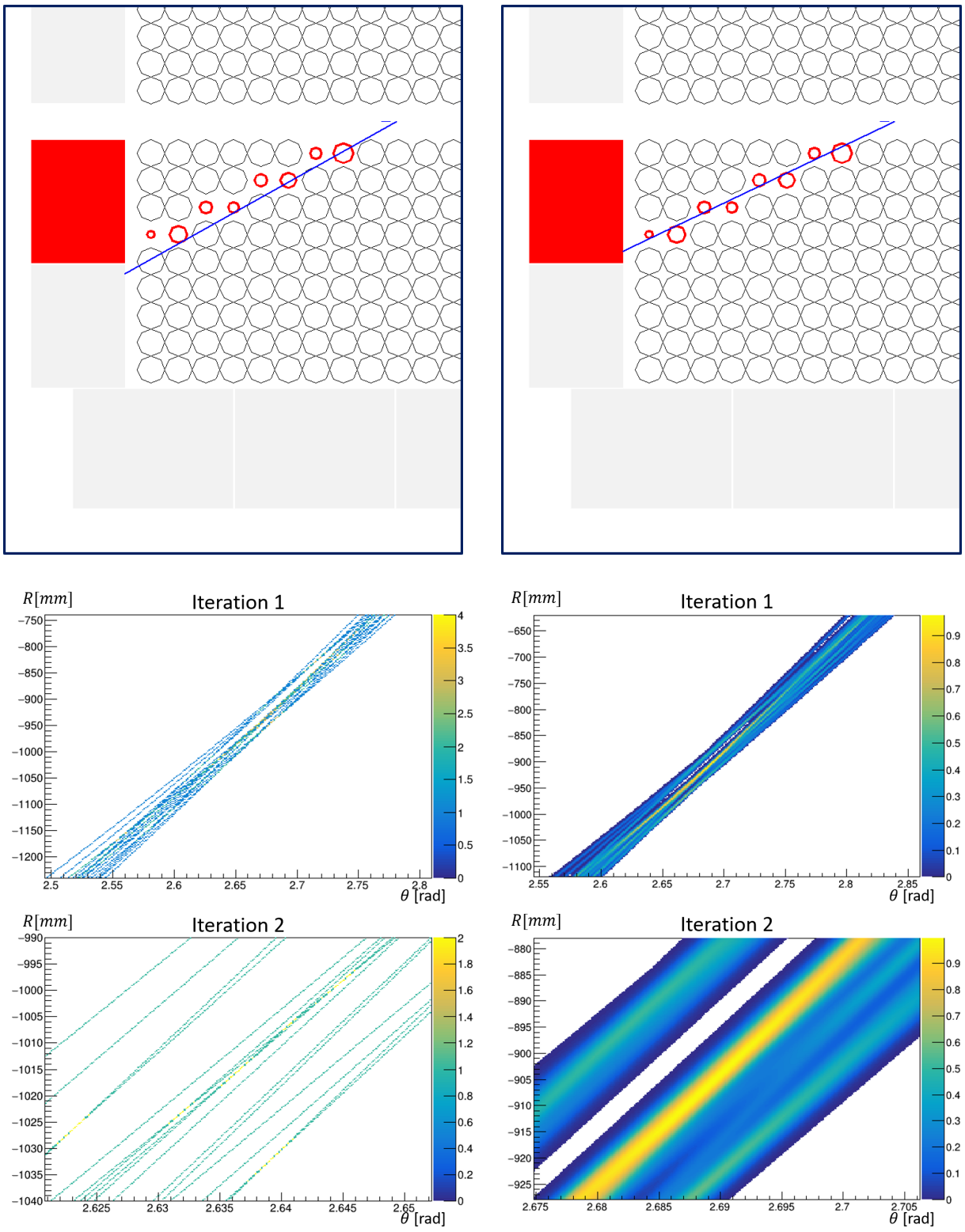

Figure 4.12: A comparison of reconstruction of event 3 from run 728 by both algorithms and sinograms from 2 out of the 4 iterations used. The left plots show reconstruction and sinograms using the original basic reconstruction. The right plots show reconstruction and sinograms obtained from the reconstruction with uncertainties.

The Legendre image corresponding to a single value r_i will dispose of such weight as well. This change results into a Gaussian blur in the R direction of the sinograms. A demonstration of this effect can be seen in Figure 4.11.

The histogram is plotted for values of $R \in (-2500\text{ mm}, 2500\text{ mm})$ but the value of σ of each Legendre image is just 2 mm. This means that the values of such two dimensional function are negligible in almost all the (R, θ) space. Therefore, we adapted an approximation. For each tracker hit we can save a large amount of computing time by only plotting the function for radii $r \in [r_0 - 3\sigma, r_0 + 3\sigma]$. The result of the reconstruction are not affected by such approximation.

A comparison of this advanced approach (with inclusion of uncertainties) and the original simpler approach (without inclusion of uncertainties) on the reconstruction of a real event is shown in Figure 4.12.

4.7 Reconstruction of multiple track candidates

The algorithm described above improves the reconstruction, however, it is still not enough for more complex events which might produce more than one track candidates. First type of a problematic feature in an event is a kink. As briefly described in Section 3.2, when the tracked particle interacts with another particle inside the tracker, it can result in a sudden change of direction, which we refer to as "kink". In such events the trajectory of the particle does not resemble a straight line but a piecewise linear path. Therefore, the reconstructed track is composed of two or more linear segments. For reconstruction of these events it is necessary to find more complex solution based on combination of multiple candidates corresponding to these segments. Example of this is shown in Figure 4.13a.

The second type of problematic feature in an event is an ambiguity caused by symmetry of the grid of tracker cells. This ambiguity can be observed in the events with centres of all tracker

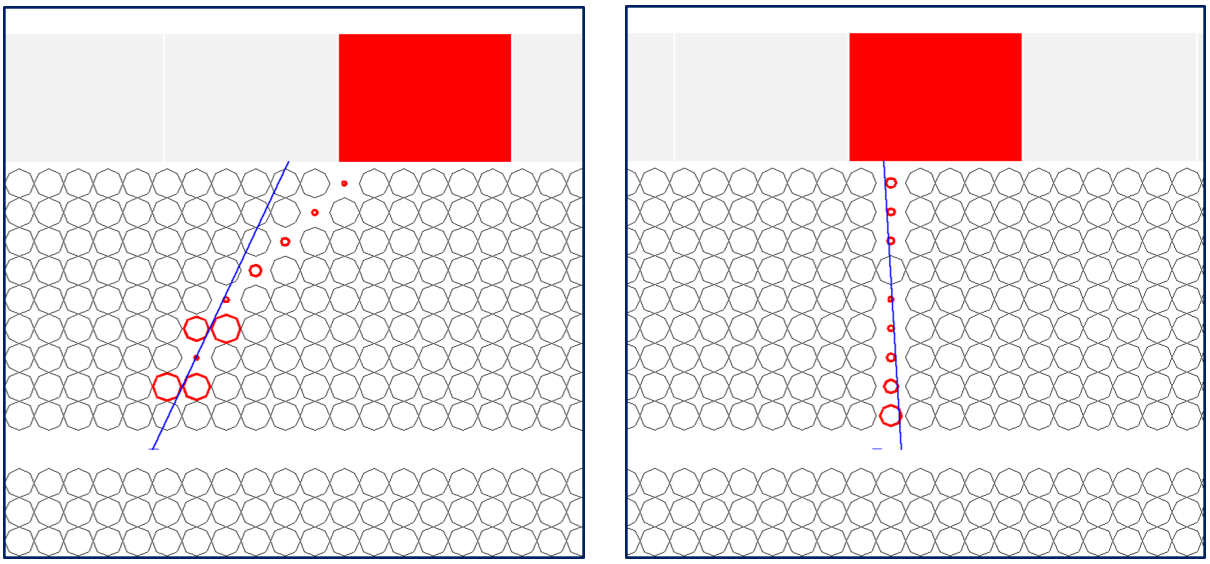

(a) event with a kink

(b) event with ambiguity

Figure 4.13: Examples of problematic events. Plot (a) shows a reconstruction of event 33 from run 728. This event contains a visible kink. Plot (b) shows a reconstruction of event 34 from run 728. This is example of an event with ambiguity.

hits aligned on a single line. This constellation of hits results in two different possible reconstructions that are equally likely – see Figure 4.13b. This specific example is from calibration run 728 which, as mentioned before, was measured with the ^{207}Bi calibration sources deployed. It is almost certain that this electron originated in the calibration source marked by the small blue rectangle in the visualization. However, to choose one or another can be done only based on the physical reasons for a given process. The mathematical tool – the reconstruction algorithm – should not prefer one candidate over the other and should be able to store both of them and make them both available for the physicist analyzing the data. For this reason we cannot use the algorithm proposed in Chapter 3 which we used to find multiple lines by removing associated tracker hits in stepwise fashion - see section 3.7. By removing the associated tracker hits we would remove the tracker hits, before we would have a chance to reconstruct the second solution. This way we would lose the second candidate in the events with ambiguity.

For these reasons, a more complicated algorithm is needed for finding more candidates. Each candidate corresponds to a position of a peak in the sinograms so the problem can be mathematically formulated as search for multiple positions of local maxima in the 2D histogram.

We do this iteratively. We start with a histogram with region $(0, \pi) \times (-2500 \text{ mm}, 2500 \text{ mm})$.

1. We divide the histogram into smaller segments.

2. A maximum is found in each segment.

3. Found maxima are filtered to keep only relatively the highest ones. In order to decide which local maxima are significant enough we set a threshold to 0.75 of the global maximum. The candidates which do not pass the threshold are ignored.

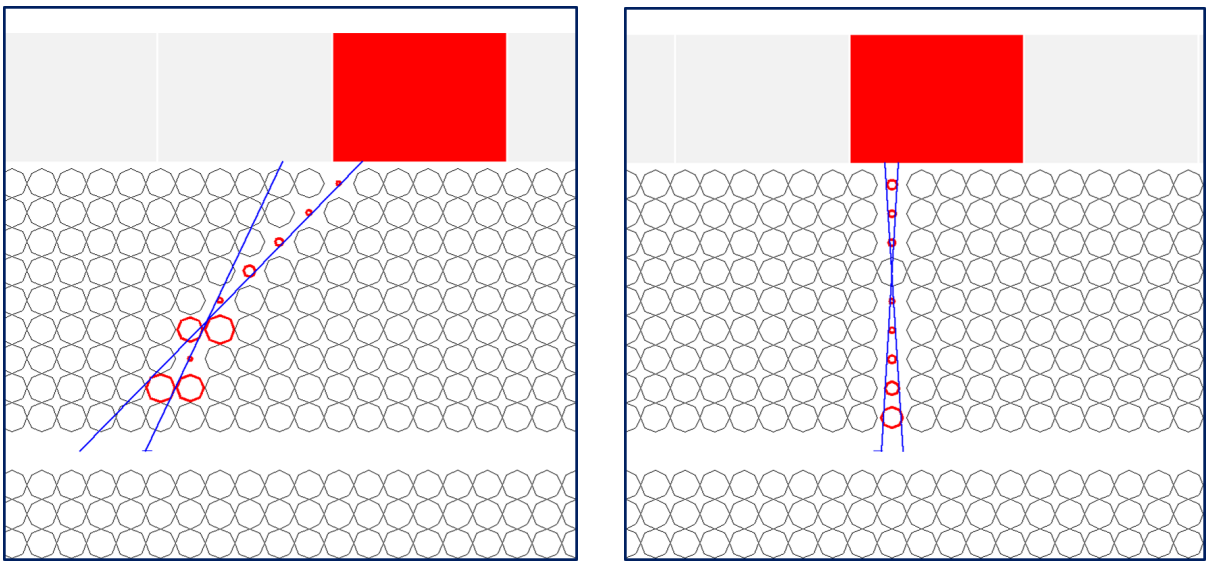

(a) event with a kink

(b) event with ambiguity

Figure 4.14: Examples of successful reconstructions of problematic events. Plot (a) shows a reconstruction of event 33 from run 728. Plot (b) shows a reconstruction of event 34 from run 728.

4. Set of new smaller histograms is defined. These are centred at the found maxima from point 3. Size of range of the new histograms is equal to the size of the segments from this iteration.

5. The process is repeated until a predefined number of iterations is reached.

Reconstruction of the two examples above with the use of this advanced search algorithm is shown in Figure 4.14. Event 34 (an event with ambiguity) is reconstructed successfully. However, to fully reconstruct event 33 as one continuous piecewise linear path instead of two separate candidates, we would need additional algorithm to connect the linear segments of the track. This will be a subject of future research.

4.8 Reconstruction of z coordinates

The final piece of the reconstruction process is the reconstruction of the vertical component. In comparison to the horizontal part of the problem, this part is simpler. We have implemented least square method for this task.

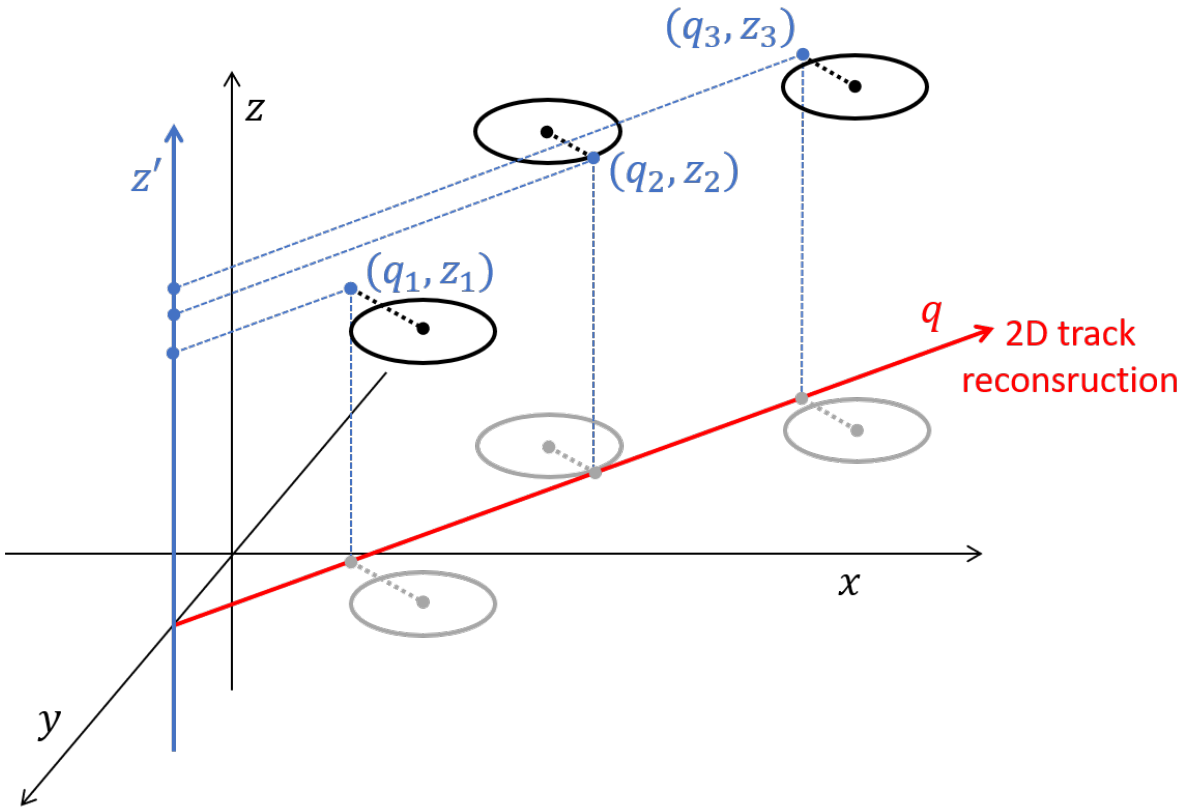

Figure 4.15: Demonstration of projection of tracker hits into new coordinate system (q, z'). Axis q is equal to a line from 2D reconstruction. Axis z' has the same direction as the original axis z. New origin is given by the intersection of axes q and y.

The reconstruction algorithm is simple:

1. The problem is solved in the horizontal plane (x, y) using the designed algorithm above which provides a reconstruction candidate in form of a line $y = ax + b$.

2. New coordinate system (q, z') is introduced (Figure 4.15). New horizontal axis q is given by the direction the found 2D reconstruction candidate. Axis z' has the same direction as the original axis z. New origin is given by the intersection of axes q and y.

3. For each tracker hit, the closest point of this hit to the plane (q, z') is orthogonally projected onto this plane. This way we obtain a set of point (q_i, z_i) in (q, z') plane.

4. Least square method is applied on points (q_i, z_i) giving us the missing parameters c and d from description of the line

$$\begin{aligned} y &= ax + b \\ z &= cx + d. \end{aligned} \tag{4.4}$$

An example of a 3D visualization of a fully reconstructed event is shown in Figure 4.16.

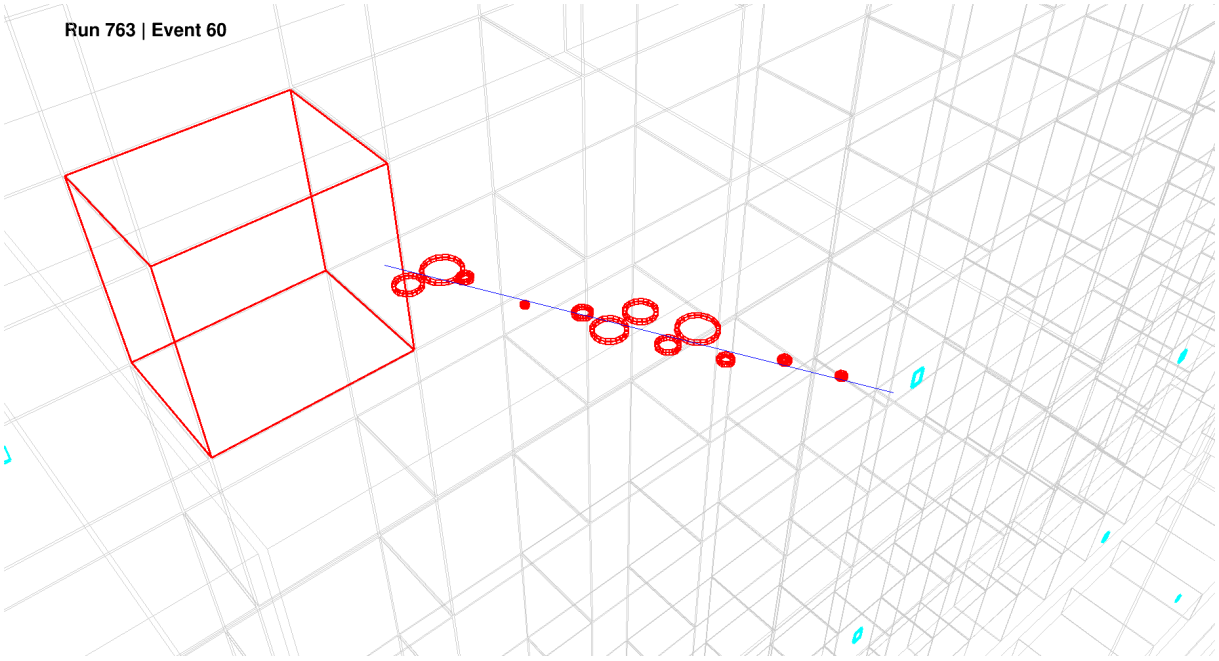

Figure 4.16: Fully reconstructed event 60 from run 763.

4.9 Final remarks and outlook

In order to fully reconstruct SuperNEMO real data events we had to overcome several problems. First, we had to convert raw detector data into more convenient data structure with the relevant values such as hit radii and hit heights. We saved them in a form of objects of dedicated C++ library TKEvent written by us. The library offers tools for 2D and 3D visualizations and to work with this data structure. In the future, this library will be updated to include more sophisticated methods as well as other algorithms. For example algorithm for energy calibration of the calorimeter which is currently being developed by Filip Koňařík.

We implemented simplified model to describe uncertainties due to presence of measurement errors in the real data. This simplified model will be replaced in the future with an advanced

drift model that will include realistic uncertainties and angular dependency when such model will be available. This will improve the quality and reliability of the reconstruction.

Finally, we designed advanced reconstruction algorithm for finding multiple solutions to reconstruct more complex event such as events with ambiguities and kinks. Additional algorithm for joining found solutions into multi-segment tracks is still needed to fully reconstruct certain events.

Another improvement can be done by maximizing used information from the tracker. At the moment, only part of the available timestamps are used to determine values of hit radii r_i as discussed in Section 4.1. By using other timestamps for tracker hits that lack the timestamps currently used, we could increase the chances of successful reconstruction.

A great opportunity for an improvement of the reconstruction lies in the use of maximum likelihood method, which will be a subject of future research. Using likelihood function could be used for better evaluation of the quality of found reconstruction candidates. Another upside of this approach could be the possibility to determine uncertainties of the parameters of a found solution which would be a crucial information later for a data analysis.

Conclusion

The Standard Model is the most accurate description of the subatomic world. Despite its great success over the last half century, it has its limitations. To create an even better model, we need to look for new physics that is not included in the SM. One promising route to new physics is the study of the neutrino. The experimental confirmation of the existence of neutrino oscillation had major implications. First, it proved the existence of new physics not included in the SM. Second, it highlighted an important question about the nature of neutrinos. Namely, what are the values of the three neutrino mass states. The values of the neutrino masses could be obtained by studying the decay of $0\nu\beta\beta$. This is because the half-life of $0\nu\beta\beta$ decay depends on these values.

In the search for the $0\nu\beta\beta$ decay, the SuperNEMO experiment stands out for its unique tracko-calo design. The separation of the detector into a tracking detector and a calorimeter system provides background rejection capabilities unmatched by other approaches. However, to reach the full potential of this design, it is necessary to develop a reliable reconstruction algorithm. The development of such algorithm for particles with simple linear trajectories was the aim of this work.

The demonstrator is currently in the final stage of the construction. In Novemeber 2020 we took part in the construction tasks for two weeks. During these two weeks we worked on improving the gastightness of the tracking chamber (Figure 4.17). Currently, all the data acquisition parts are installed and the demonstrator is taking commissioning data.

To reconstruct the linear paths from the circular tangent hits obtained from the tracker, we took advantage of the Legendre transform. Due to the complexity of the problem, we first created a simple generator of perfect simulated tracker data without measurement errors. We demonstrated the functionality of the Legendre transform based technique on such data and designed an iterative algorithm capable of accurately reconstructing the simulated linear paths. We have presented an extension of algorithm capable to reconstruct several tracks in one event.

Reconstructing the real data measured by the SuperNEMO demonstrator is much more difficult task. The raw SuperNEMO data do not contain the information required for reconstruction – tracker hit radii and tracker hit heights. To obtain these values, it is necessary to understand the raw data format and the additional use of a drift model. The drift model needs improvement, nevertheless, the current one is suitable for the needs of algorithm development. In order to calculate the necessary values and to work conveniently with the raw data, we have written a dedicated C++ library, TKEvent. An important feature of this library is the ability to visualise the raw data events together with their reconstructions. The TKEvent library is able to create a top projection view of the event as well as an iterative 3D model of the entire demonstrator with highlighted hits. This allows us to better understand the problems of the real data and to better analyse the functionality of the reconstruction.

Figure 4.17: Me and my colleagues working on gastightness of the tracker during September 2020.

The presence of measurement errors in the real data limited the accuracy and success of the reconstruction using the algorithm designed for simulated data. To overcome these difficulties, we implemented a simple Gaussian model to describe uncertainties of the measurement. Such model better describes the reality of the experimental measurement and it improved the reliability of the reconstruction. Another problem with the real data are complex events with more particle tracks or events with kinks. To reconstruct these events, we developed an algorithm to search for multiple reconstruction candidates. In order to compose these linear segments into multi-segment tracks, an extra research will be performed in the future. Finally, to reconstruct the vertical component of the trajectory, we made orthogonal projection of the tracker hits into a vertical plane defined by the 2D reconstruction candidate and implemented the least square method on the obtained points.

The technique based on the Legendre transform showed great potential as it is very robust to noise and missing data (e.g. from dead cells). On the other hand, its disadvantage is the computational time required, as it relies on multiple iterative searches through 2D histograms. The algorithm itself could be optimised by finding an ideal choice of parameters. This task is beyond the scope of the thesis.

Although our the technique provides good results, it can be improved further. Most importantly, the reconstruction in the horizontal plane can be significantly improved by implementing a more advanced drift model with angular dependence and realistic uncertainties of the measurement. This change will make the reconstruction more complex but it also should provide reliable results in case of more complex events. The reconstruction could also be improved even in its vertical component. The tracker hits contain 7 timestamps $t_0, ..., t_6$ which can be used to calculate the z-coordinate, but these values contain redundant information. This can be used to recover some of the tracker hits that we discarded for the reconstruction in the current version of the algorithm. Further research is needed on the correct implementation of this improvement.

An important limitation is the lack of a way to objectively evaluate the quality of the recon-

structed track. The development of such evaluation function is crucial for further progress and is a subject of future work. A promising candidate for such function seems to be the likelihood function. Additionally, likelihood function could be used to evaluate uncertainties of parameters of the obtained solutions. Furthermore, maximum likelihood method can be used for the reconstruction itself. An advantage of this approach would be the possibility to obtain the full 3D reconstruction without separating the problem into horizontal and vertical parts.

In summary, the results of the thesis confirmed that the Legendre transform has a great potential for the track reconstruction in SuperNEMO demonstrator. All work has been presented on several SuperNEMO collaboration and analysis meetings (e.g. November 2022, January 2023). The presented work has also uncovered many new ways to improve the method. These improvements will be studied as apart of the future research beyond the scope of the thesis.

Bibliography

1. Falconer, I. Corpuscles, Electrons and Cathode Rays: J. J. Thomson and the 'Discovery of the Electron'. *The British Journal for the History of Science* **20,** 241–276 (1987).
2. Abe, F. *et al.* Observation of Top Quark Production in $\overline{p}p$ Collisions with the Collider Detector at Fermilab. *Phys. Rev. Lett.* **74,** 2626–2631 (14 Apr. 1995).
3. Kodama, K. *et al.* Observation of tau neutrino interactions. *Physics Letters B* **504,** 218–224. ISSN: 0370-2693 (2001).
4. Aad, G. *et al.* Observation of a new particle in the search for the Standard Model Higgs boson with the ATLAS detector at the LHC. *Physics Letters B* **716,** 1–29 (Sept. 2012).
5. Cush, M. *Standard Model of Elementary Particles* 2019. `https://en.wikipedia.org/wiki/File:Standard_Model_of_Elementary_Particles.svg`.
6. Zwicky, F. Die Rotverschiebung von extragalaktischen Nebeln. *Helv. Phys. Acta* **6,** 110–127 (1933).
7. Pauli, W. Dear radioactive ladies and gentlemen. *Phys. Today* **31N9,** 27 (1978).
8. Cowan, C. L. *et al.* Detection of the free neutrino: A Confirmation. *Science* **124,** 103–104 (1956).
9. Danby, G. *et al.* Observation of High-Energy Neutrino Reactions and the Existence of Two Kinds of Neutrinos. *Phys. Rev. Lett.* **9,** 36–44 (1 July 1962).
10. Cleveland, B. T. *et al.* Measurement of the Solar Electron Neutrino Flux with the Homestake Chlorine Detector. *The Astrophysical Journal* **496,** 505 (Mar. 1998).
11. Gribov, V. & Pontecorvo, B. Neutrino astronomy and lepton charge. *Physics Letters B* **28,** 493–496. ISSN: 0370-2693 (1969).
12. Lipari, P. *Introduction to neutrino physics* in *1st CERN-CLAF School of High-Energy Physics* (May 2001), 115–199.
13. Fukuda, Y. *et al.* Evidence for Oscillation of Atmospheric Neutrinos. *Phys. Rev. Lett.* **81,** 1562–1567 (8 Aug. 1998).
14. Goeppert-Mayer, M. Double Beta-Disintegration. *Phys. Rev.* **48,** 512–516 (6 Sept. 1935).
15. Inghram, M. G. & Reynolds, J. H. Double Beta-Decay of Te^{130}. *Phys. Rev.* **78,** 822–823 (6 June 1950).
16. Elliott, S. R. *et al.* Direct evidence for two-neutrino double-beta decay in ^{82}Se. *Phys. Rev. Lett.* **59,** 2020–2023 (18 Nov. 1987).
17. Volkmer, J. *Prospects of the Investigation of EC/Beta+ Decays With the COBRA Experiment* 2018.

18. Furry, W. H. On Transition Probabilities in Double Beta-Disintegration. *Phys. Rev.* **56,** 1184–1193 (12 Dec. 1939).

19. Avignone, F. T. *et al.* Next generation double-beta decay experiments: metrics for their evaluation. *New Journal of Physics* **7,** 6 (Jan. 2005).

20. Klapdor-Kleingrothaus, H. V. *et al.* Latest results from the HEIDELBERG-MOSCOW double beta decay experiment. en. *Eur. Phys. J. A* **12,** 147–154 (Oct. 2001).

21. Guiseppe, V. E. *et al. The MAJORANA Neutrinoless Double-Beta Decay Experiment* in *2008 IEEE Nuclear Science Symposium Conference Record* (IEEE, Dresden, Germany, Oct. 2008).

22. Ackermann, K.-H. *et al.* The Gerda experiment for the search of $0\nu\beta\beta$ decay in 76Ge. en. *Eur. Phys. J. C Part. Fields* **73** (Mar. 2013).

23. Guinn, I. S. & Lopez-Castaño, J. M. *Current status of LEGEND: Searching for Neutrinoless Double-Beta Decay in ^{76}Ge: Part I* 2019. arXiv: 1912.03307 [nucl-ex].

24. New Limit for Neutrinoless Double-Beta Decay of ^{100}Mo from the CUPID-Mo Experiment. *Phys. Rev. Lett.* **126,** 181802 (18 May 2021).

25. Arnaboldi, C. *et al.* CUORE: a cryogenic underground observatory for rare events. *Nuclear Instruments and Methods in Physics Research Section A: Accelerators, Spectrometers, Detectors and Associated Equipment* **518,** 775–798. ISSN: 0168-9002 (2004).

26. Beeman, J. W. *et al.* Current status and future perspectives of the LUCIFER experiment. *Adv. High Energy Phys.* **2013,** 1–15 (2013).

27. Auger, M. *et al.* The EXO-200 detector, part I: detector design and construction. *Journal of Instrumentation* **7,** P05010 (May 2012).

28. collaboration, T. K.-Z. *et al.* The nylon balloon for xenon loaded liquid scintillator in KamLAND-Zen 800 neutrinoless double-beta decay search experiment. *Journal of Instrumentation* **16,** P08023 (Aug. 2021).

29. Flack, R. L. & Collaboration, N.-3. Results from NEMO-3. *Journal of Physics: Conference Series* **136,** 022032 (Nov. 2008).

30. Probing new physics models of neutrinoless double beta decay with SuperNEMO. en. *Eur. Phys. J. C Part. Fields* **70,** 927–943 (Dec. 2010).

31. Arnold, R. *et al.* Measurement of the distribution of ^{207}Bi depositions on calibration sources for SuperNEMO. *Journal of Instrumentation* **16,** T07012 (July 2021).

32. Macko, M. *SuperNEMO Experiment : Study of Systematic Uncertainties of Track Reconstruction and Energy Calibration. Evaluation of Sensitivity to 0nbb with Emission of Majoron for Se-82.* PhD thesis (Dec. 2018).

33. Jeremie, A. The SuperNEMO demonstrator double beta experiment. *Nuclear Instruments and Methods in Physics Research Section A: Accelerators, Spectrometers, Detectors and Associated Equipment* **958.** Proceedings of the Vienna Conference on Instrumentation 2019, 162115. ISSN: 0168-9002 (2020).

34. Hodák, R. *et al.* Advanced plastic scintillation detectors for low-background experiments. *Journal of Instrumentation* **17,** C02005 (Feb. 2022).

35. Barabash, A. *et al.* Calorimeter development for the SuperNEMO double beta decay experiment. *Nuclear Instruments and Methods in Physics Research Section A: Accelerators, Spectrometers, Detectors and Associated Equipment* **868,** 98–108. ISSN: 0168-9002 (2017).

36. Alexopoulos, T. *et al.* Implementation of the Legendre Transform for track segment reconstruction in drift tube chambers. *Nuclear Instruments and Methods in Physics Research Section A: Accelerators, Spectrometers, Detectors and Associated Equipment* **592,** 456–462. ISSN: 0168-9002 (2008).

37. Alexopoulos, T. *et al.* Track reconstruction through the application of the Legendre Transform on ellipses (May 2016).

38. Brun, R. & Rademakers, F. ROOT — An object oriented data analysis framework. *Nuclear Instruments and Methods in Physics Research Section A: Accelerators, Spectrometers, Detectors and Associated Equipment* **389.** New Computing Techniques in Physics Research V, 81–86. ISSN: 0168-9002 (1997).

39. Křižák, T. *TKEvent* `https://github.com/TomasKrizak/TKEvent`.

Appendix A

Derivation of the Legendre transform formula

In Section 3.4 it was discussed that application of the Legendre transform on a convex function f (defined on interval I) provides its Legendre image $g(p)$. Additionally, if function f is differentiable and its derivative f' can be inverted, the Legendre image $g(p)$ describes all tangent lines in form $y = px - g$ that are tangent to the function f. Let us now derive the equation 3.1 which can be used to transform the function f into its Legendre image $g(p)$:

$$g(p) = px(p) - f(x(p)). \tag{A.1}$$

First, let us consider function f defined on interval I that fulfills the conditions above. A demonstration is shown in Figure A.1.

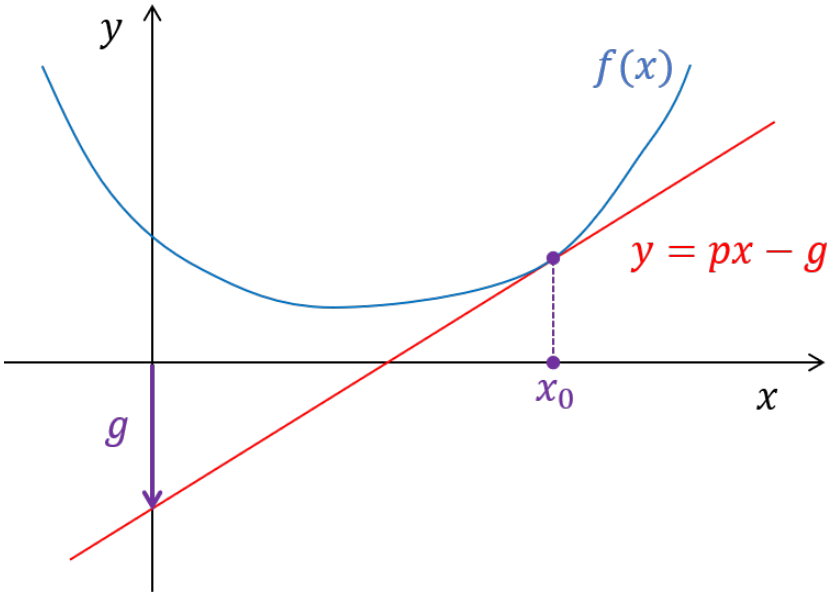

Figure A.1: A demonstration of a convex function $f(x)$ and its tangent line $y = px - g$ at point x_0.

For each point $x_0 \in I$ we will obtain parameters p, g such that they describe a tangent line at that point x_0 in form $y = px - g$. Note that the parameter g represents a negative intercept.

To satisfy the condition of tangentiality the values and derivatives of the function f and the tangent line $y = px - g$ must be equal at the point x_0. In other words, the following equations must hold:

$$\begin{aligned} f(x_0) &= x_0 p - g \\ f'(x_0) &= p. \end{aligned} \tag{A.2}$$

This gives us a unique description:

$$\begin{aligned} p &= f'(x_0) \\ g &= x_0 f'(x_0) - f(x_0) \end{aligned} \tag{A.3}$$

This holds for every $x_0 \in I$, which allows us to define parameters p and g as functions of x:

$$\begin{aligned} p(x) &= f'(x) \\ g(x) &= x f'(x) - f(x), \end{aligned} \tag{A.4}$$

where $x \in I$.

To express g as a function of p we must express x as a function of p. This can be done if $f'(x)$ is reversible. In this case

$$x(p) = (f')^{-1}(p). \tag{A.5}$$

If we plug Equation A.5 in Equations A.4 we obtain the formula:

$$g(p) = px(p) - f(x(p)). \tag{A.6}$$

In Section 3.4 we define Legendre transform only for convex functions. This is because Legendre image $g(p)$ is a function of the derivative of the original function $f(x)$. This means that this function must have different value of derivative at every point. This condition is fulfilled if the derivative is monotone. It is possible to define Legendre transform for concave functions as well as convex but it is usually defined only for convex functions. We stick to the usual definition and in case of concave functions we simply apply the transformation on a convex function $f^* = -f$.